

The Host Galaxies of Rapidly Evolving Transients in the Dark Energy Survey

P. Wiseman¹★, and Other Authors^{1,2,3},
(The DES Collaboration)

¹*School of Physics and Astronomy, University of Southampton, Southampton, SO17 1BJ, UK*

²*Other Institutions*

Accepted XXX. Received YYY; in original form ZZZ

ABSTRACT

Rapidly evolving transients (RETs), also termed fast blue optical transients (FBOTs), are a distinct class of astrophysical event. They are characterised by lightcurves that decline much faster than standard supernovae (SNe), span vast ranges in peak luminosity and can be seen to redshifts greater than 1. Their evolution on fast timescales has hindered high quality follow-up observations, such that their origin and explosion/emission mechanism remains unexplained. In this paper, we investigate the host galaxies of the largest RET sample to date from the Dark Energy Survey (DES). Using deep-stacked photometry and emission-lines from OzDES spectroscopy, we derive host galaxy stellar masses and star-formation rates (SFRs) for 49 hosts, and metallicities for 44. We find that RETs explode almost exclusively in star-forming galaxies and are thus likely associated with massive stars. Comparing RET hosts to samples of host galaxies of other explosive transient as well as field galaxies, we find that RETs prefer galaxies with high specific SFRs, indicating a link to young stellar populations, similar to stripped-envelope SNe. RET hosts appear to show a lack of chemical enrichment, their metallicities akin to long duration gamma-ray bursts and superluminous SN host galaxies. There are no clear relationships between properties of the host galaxies and the peak magnitudes or decline rates of the transients themselves.

Key words: keyword1 – keyword2 – keyword3

1 INTRODUCTION

In the standard paradigm of stellar evolution, stars with a zero-age main sequence (ZAMS) mass above $8M_{\odot}$ are believed to explode as a result of a catastrophic collapse of their iron cores and are known as core-collapse supernovae (CCSNe). CCSNe can be split into observationally-determined subclasses based on their lightcurve and spectral evolution: SNe II display hydrogen features in their spectra that disappear after a few weeks, and are thought to occur in stars that retain a large fraction of their hydrogen envelope. Conversely, SNe Ib and Ic do not show signatures of hydrogen and are thus referred to collectively as stripped-envelope SNe (SESNe), having undergone a partial removal of their outer atmospheres. The SN IIb subclass, which shows hydrogen only at early epochs, is also commonly grouped along with SESNe. SNe IIc, with the n standing for narrow, display hydrogen lines with much lower velocities than standard SNe II, indicating their origin from the ejecta impacting on slow-moving circumstellar material (CSM). Since the turn of the century, observations of CCSNe, whose lightcurves are primarily

powered by the radioactive decay of freshly synthesised Ni-56, have been supplemented by rarer, more exotic transient classes.

Long duration gamma-ray bursts (LGRBs), although first discovered in the 1960s (Klebesadel et al. 1973), were only unequivocally linked to collapsing massive stars through their associations with broad-lined type Ic SNe (Galama et al. 1998; Hjorth et al. 2003). Thought to be caused by accretion onto a newly-formed black hole at the centre of a collapsing, rapidly-rotating massive star (e.g. Woosley 1993; Woosley & Bloom 2006; Woosley & Heger 2006), LGRBs comprise roughly 1% of all SNe Ic, themselves making up only 15% of all CCSNe (Kelly & Kirshner 2012; Graham & Schady 2016). The second exotic class of SNe is the particularly bright superluminous supernovae (SLSNe; e.g. Quimby et al. 2011; Gal-Yam 2012). Originally grouped due to their slowly-evolving lightcurves and extreme luminosity (peaking at $M_B < -21$ mag; 10-100 times brighter than regular CCSNe), recent observations have revealed a continuum of spectroscopically similar objects with peaks as faint as $M_B \sim -19$ mag (De Cia et al. 2018; Lunnan et al. 2018; Angus et al. 2019), similar to the bright end of the CCSN luminosity function (Li et al. 2011). The lightcurve evolution of SLSNe is not well described by models of Ni-56 decay, with the most popular alterna-

★ E-mail: p.s.wiseman@soton.ac.uk (PW)

tive hypothesis being the magnetic coupling of the ejecta with the spin down of a newly formed, rapidly rotating magnetar.

Along with observations of the transients themselves, host galaxies are frequently-used laboratories from which strong inferences about the progenitor stars and explosion mechanisms can be made. CCSNe are confined almost exclusively to galaxies hosting recent or ongoing star formation, due to their origin from massive stars. There are correlations between the expected progenitor mass of different sub-classes of CCSNe and host galaxy properties. On average, SESNe reside in galaxies with higher specific star-formation rates (sSFRs; James & Anderson 2006; Kelly et al. 2008), while studies of the local environments tend to show SESNe to explode closer to [HII] regions than SNe II, indicating that the progenitors are younger and more massive than the various sub-classes of hydrogen-rich SNe II (e.g. Galbany et al. 2018). More extreme events tend to occur in galaxies low in mass and high in sSFR, with both GRBs (e.g. Fruchter et al. 2006; Le Floch et al. 2006; Levesque et al. 2010; Krühler et al. 2015; Vergani et al. 2015; Perley et al. 2016a; Palmerio et al. 2019; Taggart & Perley 2019) and to an even greater degree SLSNe (e.g. Neill et al. 2011; Lunnan et al. 2014; Leloudas et al. 2015; Angus et al. 2016; Schulze et al. 2018; Taggart & Perley 2019) exhibiting this association.

The chemical composition of the interstellar medium (ISM) is an important consideration when comparing host galaxy properties. While it does not appear to play a significant role in the relative production of CCSNe (although there are some trends, with SESNe typically found in slightly less metal-rich environments than SNe II; Galbany et al. 2018), it appears to be vitally important in the production of LGRBs and SLSNe. Theory predicts that the production of a LGRB should only be possible in stars with a metallicity of $Z/Z_{\odot} \leq 0.3$ (Woosley 1993) in order for the likely Wolf-Rayet or blue supergiant progenitors not to lose their outer atmospheres through metal-driven winds, thus conserving sufficient angular momentum to power the black-hole-driven jet or rapidly rotating magnetar. Many LGRB host galaxy studies have indeed revealed a metallicity threshold to be observed between 0.5 and 1 times the solar value (e.g. Stanek et al. 2006; Modjaz et al. 2008; Krühler et al. 2015; Perley et al. 2016a; Japelj et al. 2016; Vergani et al. 2017), although this is not a rigid cut. SLSN host galaxies also appear to be lower in metallicity than would be expected for their stellar mass, with a suppression of SLSN production at a value around half-solar (Lunnan et al. 2014; Chen et al. 2016; Perley et al. 2016b). They also require a particularly high sSFR, suggesting that they are explosions of very young, rapidly rotating massive stars.

Recently, inspection of high-cadence, large-area survey data sets have revealed yet more exotic transients that are less easy to explain with conventional models. Drouot et al. (2014) discovered a class of rapidly evolving transients (RETs; also termed ‘Fast Blue Optical Transients’ - FBOTs or ‘Fast Evolving Luminous Transients’ - FELTs) in the Pan-STARRS survey (PS1). Arcavi et al. (2016) discovered three rapidly rising, highly luminous objects in the Supernova Legacy Survey (SNLS) and one in the Palomar Transient Factory (PTF), of which one (SNLS04D4ec) declines rapidly like the PS1 sample. Pursiainen et al. (2018) expanded the known number of RETs to beyond 80 with their sample from the Dark Energy Survey (DES), spanning a redshift range of ~ 0 to > 1 . A further sample of five objects has been discovered by the Hyper Suprime-Cam Subaru Strategic Program (SSP) Transient Survey (Tampo et al. 2020). RETs typically rise to peak brightness in less than 10 days, and decline to 10% of their peak brightness within 30 days, much faster than typical SNe. The photometric measurements of the PS1 and DES RETs seem to be well described by

simple expanding blackbodies, although a handful show declining photospheric radii from the outset. Due to the rapid nature of their lightcurves and location at high-redshift, spectral coverage is sparse and signal-to-noise ratio (SNR) is low, such that there has not yet been a conclusive detection of absorption or emission features from the transients and thus the physical mechanism responsible for their rapid evolution remains unexplained.

There are a limited number of events detected in the local Universe whose properties are consistent with the RETs seen in the samples of PS1 and DES at cosmological distances, the most widely studied of which is AT2018cow (e.g. Prentice et al. 2018; Perley et al. 2019). The transient declined from its discovery, with constraints on a 1 day rise time, and across the full range of observed wavelengths did not resemble any known SN, GRB afterglow, or kilonova (KN; Ho et al. 2019). There are myriad explanations for the power source of AT2018cow touted in the literature, including: magnetars (Mohan et al. 2020); electron capture collapse of merged white dwarfs (Lyutikov & Toonen 2019); a tidal disruption event (TDE) of a white dwarf (Kuin et al. 2019) or of a main sequence star by an intermediate mass black hole (Perley et al. 2019); common envelope jets supernova (CEJSN; Soker et al. 2019); or a wind-driven transient (Uno & Maeda 2020). Other nearby rapid transients include the local fast-declining SN-like transient (McBrien et al. 2019) which is explained by the destruction of a white dwarf, and KSN-2015K (Rest et al. 2018) whose fast rise and decline is explained by the shock of an SN running into previously-expelled material. It is currently unclear whether these transients do indeed represent the local analogues of the DES and PS RETs.

In this paper, we present the first comprehensive study of the host galaxies of RETs. We make use of the final DES sample, which builds on Pursiainen et al. (2018) using the final year of data as well as more refined discovery techniques. Using the deep DES photometry from Wiseman et al. (2020) and spectra from OzDES (Lidman et al. 2020) we derive host galaxy properties in order to compare them to samples of CCSNe, LGRBs, and SLSNe, as well as the individual local rapid transients. For clarity, we will use the term RET to refer only to events in the high-redshift samples of DES and PS1.

The order of the paper is as follows: in Section 2 we introduce the full DES RET sample and describe the host galaxy observations in Section 3. The analysis methods and results are described in Sections 4 and 5 respectively, before a discussion (Section 6) and conclusion (Section 7). Where applicable, we adopt a spatially flat Λ CDM cosmology with the parameters $H_0 = 70 \text{ km s}^{-1}$ and $\Omega_M = 0.3$.

2 SAMPLE SELECTION

We derive our sample from the 106 RETs discovered in the 5-year DES-SN transient survey. This number expands upon the 72 of P18. The first reason for the increased sample size is the use of the 5th year of DES-SN, where P18 were only able to make use of the first four years. By imposing the P18 selection criteria on season 5, the sample is increased to 92 objects. The second reason is an update to the sample selection technique, which adds a further 14 transients.

2.1 Improvements to the search method

The original method of finding RETs in the DES-SN data (and presented in P18) was designed to be simple and used light curve modelling with Gaussian and linear fits. The simplistic method made

Table 1. Host galaxy information for the 49 RETs with a host galaxy redshift. A full-length, machine-readable version of this table is available in the online version of the manuscript.

Transient name	RA (J2000)	Dec (J2000)	m_r^a (AB)	z	Survey	Exposure time ^b (hours)
DES13C3avkj	51.97076	-27.52792	24.07937	0.04534	^c	OzDES -
DES13X3gms	35.80095	-4.49384	23.02264	0.06436	0.64792	OzDES 6.58333
DES13C1tgd	54.06436	-27.63867	20.30968	0.05848	0.19647	OzDES 10.16667
DES13C3abtt	52.62108	-28.16151	21.50529	0.03508	^d	- -
DES13S2wxf	41.61268	-0.02634	21.31219	0.03266	0.56985	OzDES 5.41639
DES13X1hav	35.03245	-5.11022	23.63452	0.07752	0.58236	OzDES 4.00000
DES13C3smn	51.97112	-28.08362	25.30041	0.06023	^c	OzDES -
DES13X3nyg	36.99228	-3.91327	23.38744	0.06173	0.71205	OzDES 45.50000
DES13X3gmd	36.50409	-4.21949	22.90614	0.05419	0.78082	OzDES 13.91667
DES13C3bcok	53.02711	-28.62476	18.61674	0.02560	0.34577	LADUMA
DES13X3afjd	37.00386	-4.58049	20.75298	0.05737	^d	- -
DES13C1acmt	54.32925	-26.83371	23.18742	0.04422	^c	OzDES -
DES13X3kgm	36.50380	-4.86636	26.46803	0.18709	^d	- -
DES13C3uig	52.94416	-27.58544	22.17966	0.03116	0.67346	ACES
DES13C3nxi	51.96356	-28.35720	24.99276	0.05177	^c	OzDES -
DES13C3asvu	52.83670	-27.36071	22.46669	0.02874	^d	- -
DES13X3pby	36.33330	-5.31408	23.82628	0.04671	^c	OzDES -
DES13X3aakf	35.71205	-4.69915	25.47453	0.09478	^c	OzDES -
DES13X2wvv	34.86526	-6.71603	21.89573	0.02567	0.47503	OzDES 4.50000
DES13X2oyb	35.31056	-5.67893	22.91589	0.06115	^c	OzDES -
DES13X3alnb	37.18496	-5.14232	25.04147	0.06167	^c	OzDES -
DES15X3atd	35.84011	-4.29142	23.87686	0.05432	^c	OzDES -
DES14S2anq	41.27776	-0.74529	17.57076	0.03648	0.05211	OzDES 0.75000
DES14E2xsm	9.67624	-43.58736	23.39163	0.04458	^c	OzDES -
DES14X1bnh	33.74902	-4.79254	21.95260	0.03597	0.82982	OzDES 3.50000
DES14E1aqi	8.73970	-43.40182	25.61559	0.23708	^d	- -
DES15S1ffi	43.18790	-0.88620	20.98517	0.02950	0.44739	OzDES 2.33333
DES14C3gzj	52.57168	-28.14019	26.04181	0.10494	^d	- -
DES14X3pko	36.90824	-3.69642	24.48291	0.06326	^d	- -
DES15S1fil	42.78846	-0.19747	20.95918	0.03719	0.22647	OzDES 0.66667
DES14C1jnd	54.35153	-27.49300	24.33143	0.08524	^c	OzDES -
DES14X3pkl	37.21103	-4.80741	22.40853	0.06026	0.29537	OzDES 5.16667
DES13X3npb	36.64218	-4.13381	20.79328	0.05336	0.49542	OzDES 5.16667
DES15X2ead	36.48913	-6.45118	20.08582	0.03290	0.23175	OzDES 2.00000
DES15C3edw	52.55235	-27.71022	22.69331	0.03227	^d	- -
DES14S2plb	41.85667	-1.61811	18.38419	0.03463	0.11531	OzDES 2.00000
DES14S2pli	41.22837	-1.09830	20.86839	0.03093	0.35478	OzDES 3.41667
DES15X3kyt	36.27500	-5.41103	24.74520	0.07892	^d	- -
DES14C3tvw	53.32230	-27.90621	21.31841	0.02516	0.70390	ACES
DES14C3tnz	52.86248	-28.51318	22.26137	0.03386	0.70452	OzDES 5.79361
DES15X3mxf	36.74009	-5.23991	22.43347	0.04552	0.43673	OzDES 9.83333
DES15X3nlv	36.04464	-5.02735	25.26349	0.08375	^d	- -
DES15C3mem	52.14216	-29.05851	20.28975	0.04590	0.61618	PRIMUS
DES15E2lmq	9.62005	-43.98734	25.65868	0.18116	^d	- -
DES15C3lpq	52.71204	-28.61319	23.28579	0.03610	0.61365	OzDES 6.16667
DES15C3lzm	52.17460	-28.23186	20.47636	0.02573	0.32690	ATLAS
DES15C3nat	52.88528	-28.72370	23.39015	0.03154	0.83929	OzDES 18.62222
DES15C3mgq	52.76901	-28.20882	22.97470	0.03194	0.23031	OzDES 8.16667
DES15E2nqh	9.73174	-43.08707	23.29709	0.03941	0.51525	OzDES 6.83333
DES15C3opk	51.66147	-28.34737	23.05209	0.03270	0.56984	OzDES 12.16667
DES15C3opp	51.73962	-28.11496	23.25950	0.04223	0.44242	OzDES 16.75000
DES15C3pbi	52.23620	-28.00223	25.10028	0.05470	^d	- -
DES16E2pv	9.20875	-43.52782	23.00100	0.05043	0.72608	OzDES 6.00000
DES16S1bbp	43.26389	0.37149	21.42883	0.04524	0.19018	OzDES 3.33333
DES15X3oma	36.74617	-5.11040	24.94606	0.07447	^d	- -
DES16C3bor	52.48232	-28.04256	23.83923	0.03711	^c	OzDES -
DES16C1bde	54.30149	-26.75840	24.96313	0.09485	^d	- -
DES16X3wt	36.23751	-5.54488	26.90234	0.28423	^d	- -
DES16X3cxn	36.83044	-4.95100	23.05257	0.04442	0.58464	OzDES 12.83333
DES16X2bke	36.00989	-7.27130	25.13096	0.16403	^d	- -
DES16C1cbd	54.85826	-27.67254	20.93909	0.03048	0.54108	OzDES 7.20000
DES16C3cdd	52.42731	-27.14317	24.27019	0.05040	^d	- -
DES16E1bir	7.74444	-42.97696	24.74236	0.07595	^c	OzDES -
DES16C3auv	51.90215	-27.59087	24.39158	0.05296	^c	OzDES -
DES16C3axz	52.80904	-28.66678	20.41796	0.03716	0.22673	LADUMA
DES16X3ega	37.09820	-4.77643	19.53601	0.04874	0.25762	GAMA 1.00000
DES16X3erw	36.20545	-4.51438	22.23157	0.02865	0.45885	OzDES 2.00000
DES16X1ddm	33.82824	-4.36428	21.46049	0.04767	^c	OzDES -
DES16X3lji	35.43336	-4.68682	23.23730	0.04169	^c	OzDES -

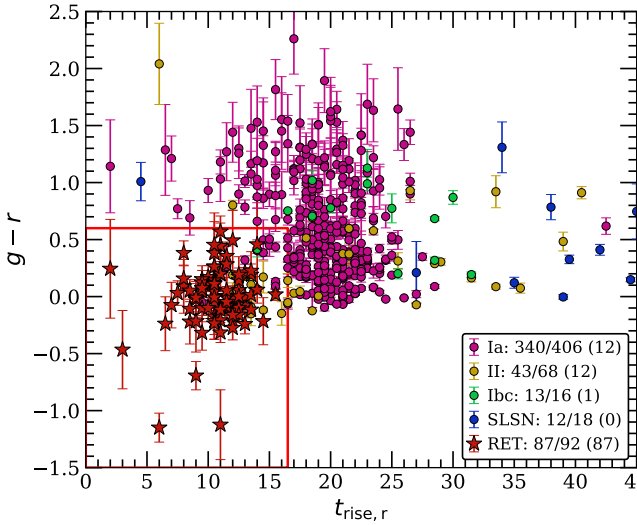


Figure 1. Observer-frame $g-r$ colour at maximum light and observer-frame r -band rise-time, derived from Gaussian Process fits to DES-SN photometry for spectroscopically confirmed SNe and P18 RETs. The location of the red box is designed to maximise the completeness and purity of RETs. The fractions in the legend refer to the number of each class of transient passing the cuts of Section 2.1 compared to the total number of that class in DES-SN, while the number in parentheses refers to the number inside the red box defining RET parameter space.

it possible to look for exotic transients without knowing their observed characteristics beforehand and resulted in a large sample of photometrically selected fast transients. However, as the search was simplistic and relied heavily on visual inspection of the available data (etc. images, light curves, host galaxy information), it is impossible to be sure how complete the sample is. For instance, due to the large redshift range within the sample it is entirely possible that distant events could have been missed due to time dilation. Here, a more sophisticated search method is presented. As only a fraction of transients in DES-SN have redshift information from host galaxy, the search must be done in the observer frame. The key features of RETs that separate them from most traditional SNe types are the fast light curve evolution and blue colour at peak. Even though both of these quantities depend on the redshift of the transient, they still seem to distinguish the fast events from traditional SN types.

To assess the unique photometric properties of RETs, we take the sample of 72 from the P18 method, updated with 20 extra objects found using that method in the fifth season of DES, along with spectroscopically confirmed SNe of types Ia, Ibc, II, and SLSNe from DES that pass the following criteria:

- (i) The transient was only detected in one DES-SN observing season.
- (ii) Maximum observed brightness in both g - and r -bands was brighter than 24 mag (in the eight ‘shallow’ DES-SN fields) or 25 mag (in the two ‘deep’ fields).
- (iii) g - and r -band observations used for the colour had to be taken within 2 days of each other in the observer frame.

Of objects passing these cuts, the RETs cluster at shorter timescales and bluer colours than other SNe, even in the observer frame. However, using photometric data points directly has several problems that can be improved. For one, measuring peak colour is problematic: DES-SN did not always observe g - and r -bands on the same or even consecutive nights, thus making it impossible to

measure the peak colour in a number of cases. Measuring rise times of 10-15 days is difficult to perform with a one week cadence when it has to be done without fitting a light curve model, hence the rise time values are spread over a wide range. To negate this issue, we use lightcurves interpolated using Gaussian (GP) as presented in Pursiainen et al. (2019). The interpolated light curves have a 0.5 day cadence and every epoch and band has a flux value, and an associated uncertainty. Using this technique, SNe Ia and RETs populate two distinct regions of $g-r$ vs. $t_{\text{rise},r}$ parameter space (Fig. 1), where $t_{\text{rise},r}$ is the time to rise from non-detection to peak r -band brightness, and the $g-r$ colour is measured at peak brightness. We define a region in this parameter space which minimises the contamination of non-RETs (purity) while maximising the total fraction of RETs (completeness). The resulting limits are $-1.5 < g-r < 0.6$ and $t_{\text{rise},r} < 16.5$, and the parameter space can be seen in Fig. 1.

We process all $\sim 30,000$ DES-SN transient candidates with GP. In order to reduce the contamination from active galactic nuclei (AGN), we use a basic convolutional neural network (CNN) classifier. We train the CNN on spectroscopically confirmed SNe of all types and on spectroscopically typed AGN, and use it to separate the sample into two photometric subtypes: AGN-like and SNe-like. The classifier returns SNe-like objects with an accuracy of 0.992 on the test set; the remaining AGN are removed by manual vetting. The SNe passing the CNN classifier are subjected to LC quality cuts, resulting in 2259 objects, of which 939 lie inside the colour and rise-time region which we defined as RETs. These objects are subject to a further set of cuts. We impose a cut based on a fit of the LC with the PSNID software (Sako et al. 2008). We use thresholds of FITPROB < 0.91 and PBAYES < 0.82 to remove highly-probably SNe Ia, which removes 46 objects from the RET parameter space. In order to further remove longer-lived SNe, the decline time to half of the peak brightness must be < 24 days. This removes 347 SNe, resulting in 546 objects remaining inside the parameter space. The final 564 transients have been visually inspected, with the majority rejected for being spurious detections, obvious multi-season variability that was not picked up by the CNN, or showing evidence for a longer timescale decline.

Using the above method recovers 87 of the 92 RETs found using the P18 technique, and adds a further 14. The five were not recovered as their GP lightcurves were fainter than the limits given above in either g or r band. We refer to the resulting sample as DES RETs. Of the 106 objects in the sample, 96 have a host galaxy detected in deep host galaxy photometry of Wiseman et al. (2020), of which 49 have a host galaxy spectroscopic redshift which we access through an internal release of the OzDES Global Redshift Catalog (GRC; v.2020_01_04). The full OzDES GRC will be available alongside the public data release detailed in Lidman et al. (2020). A further three have redshifts obtained from narrow lines observed in spectra of the transients themselves. We do not consider these three objects for the analysis, since we are unable to separate transient and host contributions to the spectra. A selection of the host galaxies can be seen in Fig. 2, centered on the location of the transient. The figure showcases the diversity of host galaxy morphologies and colours, while also displaying the limitations of ground-based observations of high-redshift, relatively small galaxies in terms of spatial resolution. Fig. 3 shows the distribution of redshifts amongst the 49 hosts for which such a measurement was possible. The effect that the redshift selection function has on the results is discussed in Section 6.1. The observational properties of the 96 detected hosts are displayed in Table 1. We highlight objects that were not presented in P18. We also highlight a small subset of objects for which the redshift

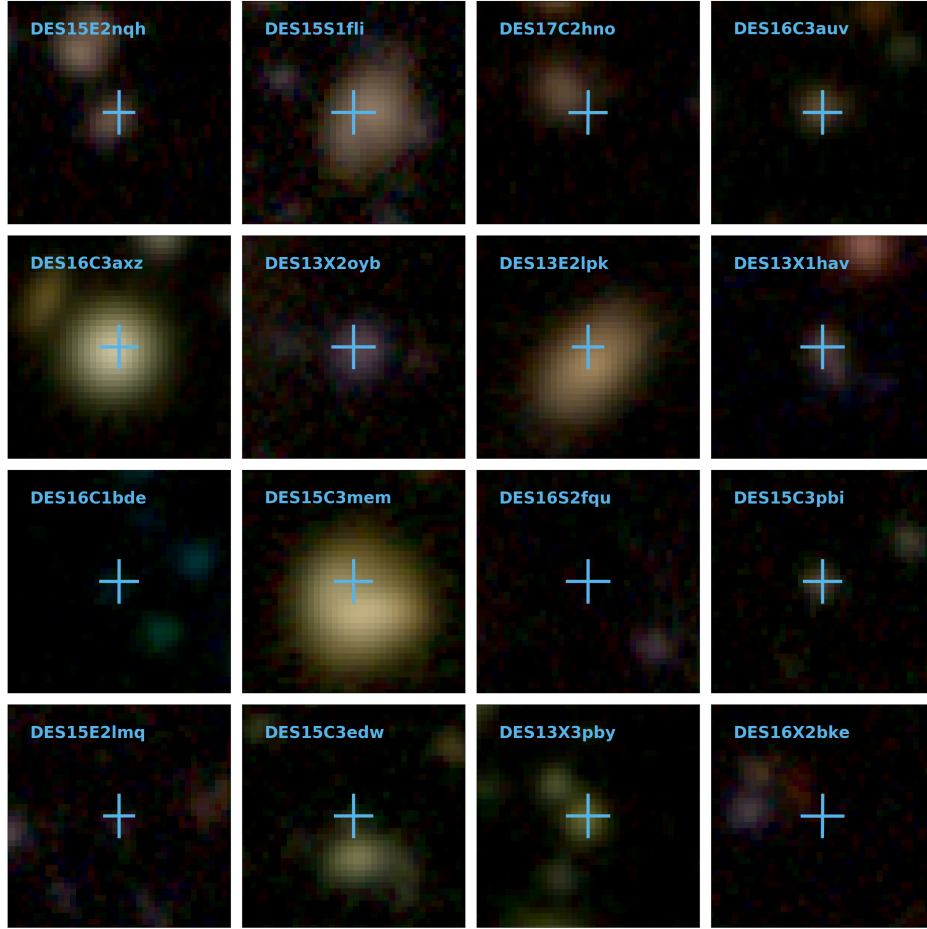


Figure 2. Selection of DES RET host galaxies in an RGB composite of the DES *gri* band deep coadds from Wiseman et al. (2020). The locations of the transients are indicated with cyan crosses. The stamps have a size of $10''$ in each direction.

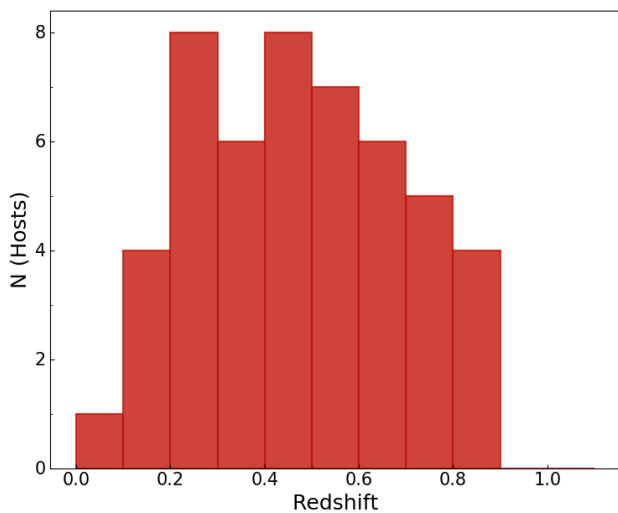


Figure 3. Redshift distribution for the host galaxies of RETs in DES for which a measurement was obtained.

2.2 Comparison samples

In order to compare the host galaxies of DES RETs to those discovered in other surveys as well as other types of explosive transient, we draw upon samples in the literature.

2.2.1 RETs

Since the DES sample of RETs is by far the largest discovered to date, there is no other large sample of RETs with which to compare host galaxy properties. Drout et al. (2014) present host galaxies of 10 RETs discovered in the Pan-STARRS survey, with measurements of stellar masses, SFRs, and metallicities. We also compare with the host galaxy of SNLS04D4ec (Arcavi et al. 2016). To this we add the low-redshift transient AT2018cow (nicknamed “The Cow”) with host galaxy photometric measurements from Perley et al. (2019) and metallicity (Pettini & Pagel 2004 O3N2) from Morokuma-Matsui et al. (2019), SN2018gep with data from Ho et al. (2019), and ZTF18abvkwla (nicknamed “The Koala”) from Ho et al. (2020).

2.2.2 SNe and GRBs

In compiling a set of comparison samples, we aim for the least biased selections possible. This requires surveys to be untargeted (they were not monitoring certain galaxies in order to search for

has taken on a new value than that presented in P18 due to further OzDES observations leading to a more accurate determination.

SNe), ideally complete, and also covering a similar redshift range to the RETs. While in practice the second and third of these criteria are difficult to achieve, particularly with the fainter CCSNe, we are able to choose comparison samples from untargeted surveys to mitigate initial selection biases.

To compare with CCSNe, we draw on the untargeted sample of 47 SNe II from the Palomar Transient Factory (PTF; Stoll et al. 2013), which is likely complete in terms of hosts (all SNe have an associated host). While this sample lies at much lower redshift than the DES RETs (a maximum of 0.18 and mean of 0.05), redshift evolution is easier to account for than unknown incompleteness. We add to this the compilation of 56 untargeted SESNe from Sanders et al. (2012), with a maximum redshift of 0.26 and a mean of 0.05. Since Sanders et al. (2012) do not report host galaxy magnitudes, stellar masses or SFRs, we cross-match the SN positions with the Sloan Digital Sky Survey (SDSS; York et al. 2000) Data Release 16 (DR16; Ahumada et al. 2019) and perform our own SED fit using the method outlined in Section 4.1. We are able to do this for 38 objects, with the others lying outside of the SDSS footprint.

We use the sample of GRB host galaxies of Krühler et al. (2015), using only galaxies with $z < 1$ in order to maintain completeness, resulting in a sample of 29 hosts with a mean redshift of 0.66. To investigate similarities with SLSNe, we use the host galaxy sample from PTF presented in Perley et al. (2016b) with a mean redshift of 0.24 and a maximum of 0.50.

The host galaxy properties of the above samples are not all derived using the same methods. In terms of SED fitting, the largest systematic offsets in derived properties are due to differences in the assumed initial mass function (IMF). Stoll et al. (2013) and Drout et al. (2014) assume a Salpeter (1955) IMF whereas all other samples considered (including those calculated in this work in Section 4.1) are determined assuming a Chabrier (2003) IMF. Stellar masses and star-formation rates derived using a Salpeter IMF are roughly ~ 1.72 times higher than those using a Chabrier IMF (Speagle et al. 2014), and we convert the Salpeter-derived values by this factor in order to compare them.

3 HOST GALAXY OBSERVATIONS

3.1 Photometry

The host galaxy photometry for the sample of RETs is taken from the catalogue of Wiseman et al. (2020), which is based upon deep coadds reaching r -band limiting magnitudes of 26.5. The coadds were created using data from all five seasons of DES-SN, but by excluding one season at a time in order for that coadd not to include contamination from the transients in that season. For this sample, the limiting magnitude for obtaining a spectroscopic redshift (Section 3.2) is ~ 24.5 , meaning that all hosts in the sample are detected with a high S/N.

3.2 Spectroscopy

Accurate redshifts for DES-SN were obtained by OzDES, a dedicated DES spectroscopic follow-up campaign based at the 3.9 m Anglo-Australian Telescope (AAT) using the AAOmega fibre-fed spectrograph and 2dF fibre positioner. The observation strategy of OzDES was to point at one of the ten DES-SN fields, and place fibres at the positions of transient hosts, continually coadding the spectra of a particular host until a redshift was obtained at which point the fibre could be allocated to a different transient. The spectra have a

resolution of 1400-1700 and a wavelength range of 3700 8800 Å, and are reduced using the OzDES pipeline which makes use of a modified version of v6.46 of the 2dfr (Croom et al. 2004) along with internal scripts. We use internal data release 7, a preliminary version of the public data release is detailed in Lidman et al. (2020). Extensive description and discussion of OzDES can be found in Yuan et al. (2015); Childress et al. (2017); Lidman et al. (2020). We also obtained redshifts for some transient hosts serendipitously as part of the Looking at the Distant Universe with the MeerKAT Array (LADUMA) survey¹, three of which are present in our sample. Objects for which the host already had a publicly available redshift were not observed with OzDES, but merged into the GRC nonetheless. Where the spectra from which those redshifts were derived are also public they are included in this analysis. These comprise the Galaxy and Mass Assembly survey (GAMA Driver et al. 2009; Baldry et al. 2018) and SDSS. In total we analyse 42 spectra, with a mean continuum signal-to-noise ratio (SNR) of 2.56/pixel. We stress that the emission lines are detected with a higher SNR than this.

4 ESTIMATING HOST GALAXY PROPERTIES

4.1 Photometric stellar parameters

To estimate the physical properties of the DES RET host galaxies, we generate synthetic photometry in the DES *griz* bands by combining the individual SEDs of simple stellar population models. We simulate a suite of synthetic galaxy star-formation histories from which we synthesise model SEDs using stellar population models from Bruzual & Charlot (2003) and a Chabrier (2003) initial mass function (IMF). The suite of models is drawn from the same distribution of parameters as used in Kauffmann et al. (2003) and similar papers (e.g. Gallazzi et al. 2005; Gallazzi & Bell 2009) and closely follows the method of Childress et al. (2013). From the synthetic SEDs we derive model magnitudes in the DES *griz* bands and compare them to the observed *Kron* magnitudes from the deep photometric catalogue of Wiseman et al. (2020). For each set of model and observed magnitudes we calculate a χ^2 value, and from these calculate a PDF for key model parameters (mass-to-light ratio M/L , from which we derive M_* , and specific star-formation rate sSFR). To estimate uncertainties, we take the values at the 16th and 84th percentiles of the resulting PDF to be our 1σ lower and upper bounds. The results are presented in Table 2. These parameters are estimated using global photometry of the entire galaxies, and thus represent the overall stellar population characteristics.

4.2 Spectroscopic gas-phase parameters

To estimate parameters from the OzDES host galaxy spectra requires several processing steps. We first apply a flux calibration by ‘mangling’ the spectrum such that the integrated flux over the wavelength ranges of the DES photometric bands matches that measured in the photometry (further details on the mangling process are provided in Swann 2020). We use a circular aperture of diameter $2''$, matching the size of the spectrograph fibres. This way the resulting spectrum is a more accurate representation of the true spectrum at that point in the galaxy. This only holds, however, for the area covered by the fibre and we note that the resulting spectrum is not necessarily representative of the galaxy as a whole. There are several

¹ <http://www.laduma.uct.ac.za>

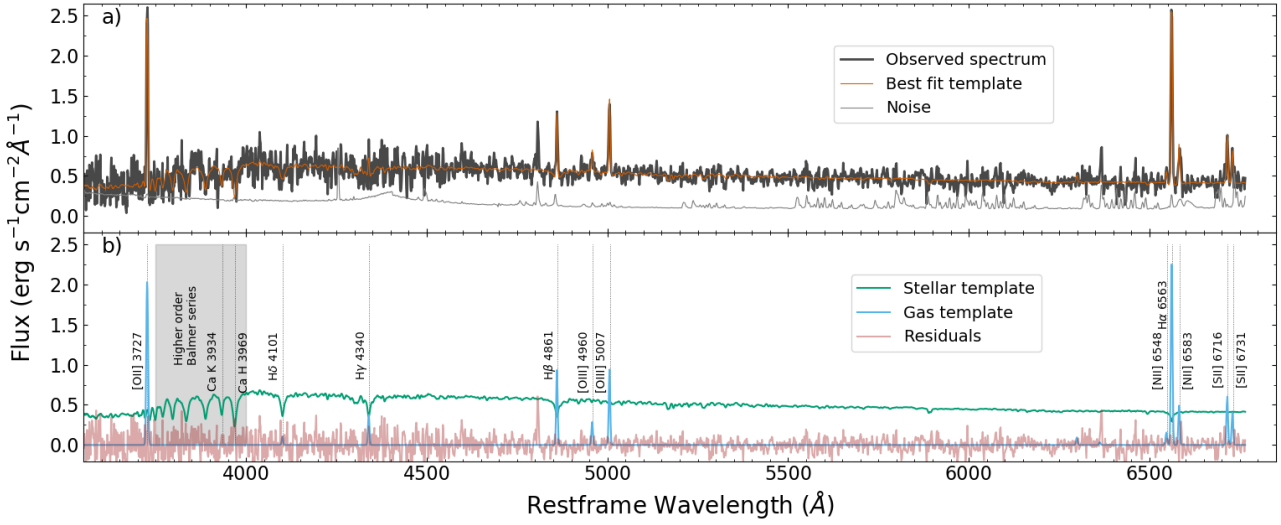


Figure 4. The spectrum of DES16C2ggt, decomposed into its constituent components according to the pPXF fit.

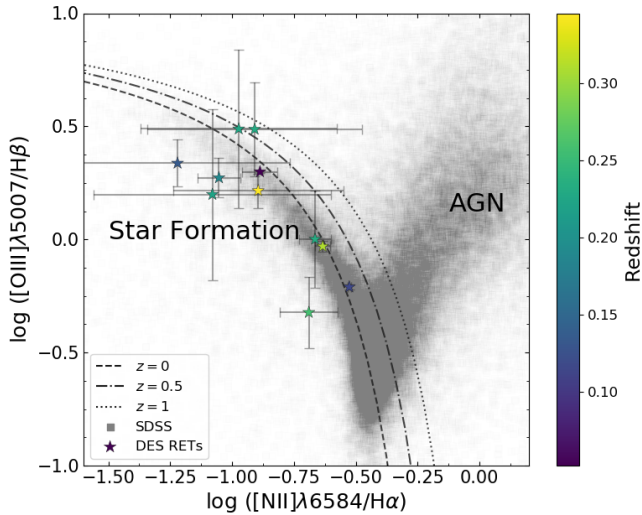


Figure 5. Baldwin-Phillips-Terlevich (BPT) diagram for RET hosts, showing that the emission lines are consistent with being generated by star formation rather than AGN activity. The three curves show the delimitation between star formation and AGN at $z = 0, 0.5, 1$ according to Kewley et al. (2013).

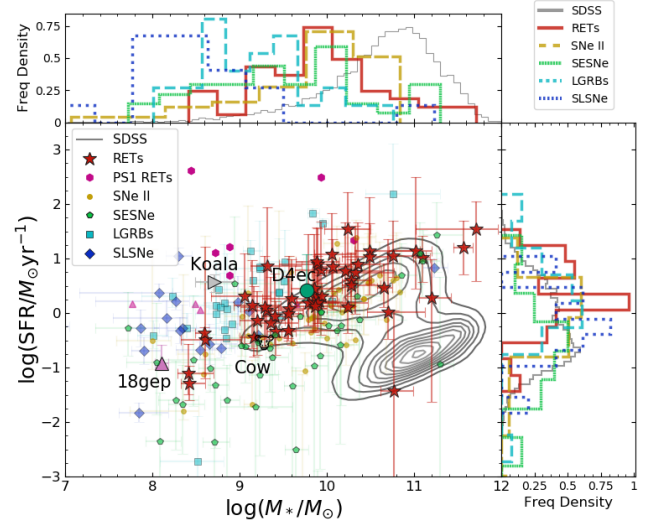


Figure 6. The SFR of RET hosts, compared to CCSNe and the low- z SDSS sample.

reasons this may not be the case, such as metallicity and age gradients or structure such as bars and discs (see e.g. Iglesias-Páramo et al. 2013, 2016), and proceed with our analysis with this caveat acknowledged.

In order to subtract the stellar component of the host galaxy spectra, we use the Penalized PiXel-Fitting software (pPXF; Cappellari & Emsellem 2004; Cappellari & Michele 2012; Cappellari 2017), using the MILES library of single stellar populations (Vazdekis et al. 2010). By subtracting the best-fitting composite stellar spectrum from the pPXF fit, we are left with a ‘gas’ spectrum, comprising the emission lines. An example of this procedure is shown in Fig. 4. We fit the emission lines with Gaussian profiles. In order to estimate the uncertainty on the emission line fluxes, we fit 10^4 realisations of the line, each time adding perturbations to the line by drawing from a Gaussian distribution based on the variance

spectrum. We take the mean and standard deviation of the resulting fits as our flux and its uncertainty, respectively.

4.3 Estimating metallicities

The most common method used to estimate the metallicity of galaxies is to use emission line ratios that have been calibrated using theoretical or empirical models in order to approximate the gas-phase oxygen abundance in the interstellar medium. Emission lines originate from regions of ionised gas, but there are a number of possible causes of this ionisation. Using the Baldwin-Phillips-Terlevich diagram (Fig. 5; Baldwin et al. 1981), we demonstrate that the emission line ratios measured in RET hosts are consistent with ionisation caused by star-formation as opposed to AGN. We note that only 11 of the 44 RET host spectra have the necessary lines to plot a BPT diagram. This is also the case for the [SII] and [OI] versions of the

Table 2. Host galaxy properties for the 49 DES RET host galaxies with redshifts and host galaxy spectra. The table is available in the online version in a machine readable format.

Transient Name	$\log(M_*)$ (M_\odot)	$\log(\text{SFR})$ ($M_\odot \text{yr}^{-1}$)	$\log(\text{sSFR})$ ($M_\odot \text{yr}^{-1} M_\odot^{-1}$)	Best	D16	PP04 N2	PP04 O3N2	KK04 R23	Average O3N2 ^b
DES13X3gms	9.41 ^{+0.27} _{-0.16}	-0.06 ^{+0.78} _{-0.51}	-9.47 ^{+0.52} _{-0.35}	8.55 ^{+0.37} _{-0.86}	-	-	-	8.55 ^{+0.37} _{-0.86}	8.22 ^{+0.35} _{-0.35}
DES13C1tgd	10.24 ^{+0.08} _{-0.09}	0.10 ^{+0.38} _{-0.47}	-10.14 ^{+0.30} _{-0.39}	8.64 ^{+0.06} _{-0.06}	8.59 ^{+0.03} _{-0.03}	8.68 ^{+0.03} _{-0.03}	-	-	8.75 ^{+0.03} _{-0.03}
DES13S2wxf	9.86 ^{+0.06} _{-0.03}	0.20 ^{+0.10} _{-0.07}	-9.57 ^{+0.04} _{-0.04}	8.58 ^{+0.27} _{-0.58}	-	-	-	8.58 ^{+0.27} _{-0.58}	8.25 ^{+0.25} _{-0.25}
DES13X1hav	9.16 ^{+0.38} _{-0.16}	-0.44 ^{+0.93} _{-0.37}	-9.60 ^{+0.55} _{-0.21}	8.51 ^{+0.39} _{-0.75}	-	-	-	8.51 ^{+0.39} _{-0.75}	8.20 ^{+0.36} _{-0.36}
DES13X3nyg	9.31 ^{+0.12} _{-0.26}	0.05 ^{+0.73} _{-0.53}	-9.27 ^{+0.32} _{-0.27}	8.46 ^{+0.12} _{-0.16}	-	-	-	8.46 ^{+0.12} _{-0.16}	8.18 ^{+0.07} _{-0.03}
DES13X3gmd	10.33 ^{+0.44} _{-0.50}	0.74 ^{+0.86} _{-0.75}	-9.59 ^{+0.42} _{-0.25}	-	-	-	-	-	-
DES13X2wvv	9.79 ^{+0.34} _{-0.14}	0.19 ^{+0.25} _{-0.43}	-9.60 ^{+0.91} _{-0.28}	8.41 ^{+0.27} _{-0.45}	-	-	-	8.41 ^{+0.27} _{-0.45}	8.16 ^{+0.16} _{-0.16}
DES14S2anq	9.41 ^{+0.23} _{-0.10}	-0.34 ^{+0.54} _{-0.43}	-9.75 ^{+0.33} _{-0.32}	8.34 ^{+0.02} _{-0.15}	8.16 ^{+0.09} _{-0.11}	8.34 ^{+0.04} _{-0.04}	8.35 ^{+0.02} _{-0.03}	8.36 ^{+0.01} _{-0.01}	8.29 ^{+0.02} _{-0.02}
DES14X1bnh	11.71 ^{+0.25} _{-0.69}	1.53 ^{+0.52} _{-0.95}	-10.18 ^{+0.26} _{-0.25}	-	-	-	-	-	-
DES15S1ffi	10.24 ^{+0.26} _{-0.27}	1.54 ^{+0.67} _{-0.94}	-8.70 ^{+0.41} _{-0.75}	8.79 ^{+0.05} _{-0.06}	-	-	-	8.79 ^{+0.05} _{-0.06}	8.44 ^{+0.06} _{-0.06}
DES15S1fil	9.20 ^{+0.32} _{-0.20}	-0.14 ^{+0.54} _{-0.64}	-9.34 ^{+0.22} _{-0.43}	8.34 ^{+0.32} _{-0.26}	8.38 ^{+0.36} _{-0.47}	8.32 ^{+0.16} _{-0.17}	8.27 ^{+0.13} _{-0.19}	8.59 ^{+0.31} _{-0.50}	8.29 ^{+0.32} _{-0.18}
DES14X3pkl	9.60 ^{+0.26} _{-0.34}	0.26 ^{+0.72} _{-0.85}	-9.34 ^{+0.46} _{-0.51}	8.37 ^{+0.13} _{-0.22}	8.20 ^{+0.09} _{-0.11}	8.48 ^{+0.06} _{-0.06}	-	-	8.52 ^{+0.07} _{-0.07}
DES13X3npb	11.02 ^{+0.18} _{-0.31}	1.14 ^{+0.35} _{-0.70}	-9.88 ^{+0.17} _{-0.39}	8.98 ^{+0.05} _{-0.05}	-	-	-	8.98 ^{+0.05} _{-0.05}	8.65 ^{+0.06} _{-0.06}
DES15X2ead	9.92 ^{+0.20} _{-0.08}	0.22 ^{+0.47} _{-0.41}	-9.69 ^{+0.27} _{-0.32}	8.47 ^{+0.13} _{-0.25}	8.23 ^{+0.09} _{-0.10}	8.48 ^{+0.05} _{-0.05}	8.52 ^{+0.08} _{-0.07}	8.67 ^{+0.33} _{-0.66}	8.45 ^{+0.16} _{-0.00}
DES14S2plb	10.36 ^{+0.25} _{-0.23}	0.89 ^{+0.77} _{-0.64}	-9.47 ^{+0.52} _{-0.40}	8.62 ^{+0.33} _{-0.33}	8.59 ^{+0.01} _{-0.01}	8.60 ^{+0.01} _{-0.01}	8.63 ^{+0.00} _{-0.00}	8.96 ^{+0.01} _{-0.01}	8.64 ^{+0.01} _{-0.01}
DES14S2pli	10.27 ^{+0.34} _{-0.39}	0.50 ^{+0.61} _{-0.73}	-9.77 ^{+0.27} _{-0.38}	8.86 ^{+0.03} _{-0.03}	-	-	-	8.86 ^{+0.03} _{-0.03}	8.52 ^{+0.04} _{-0.04}
DES14C3tnz	10.21 ^{+0.41} _{-0.22}	0.78 ^{+0.88} _{-0.60}	-9.44 ^{+0.47} _{-0.38}	8.68 ^{+0.26} _{-0.71}	-	-	-	8.68 ^{+0.26} _{-0.71}	8.33 ^{+0.28} _{-0.28}
DES15X3mxf	9.93 ^{+0.32} _{-0.30}	0.78 ^{+0.90} _{-1.08}	-9.15 ^{+0.88} _{-0.88}	8.57 ^{+0.11} _{-0.13}	-	-	-	8.57 ^{+0.11} _{-0.13}	8.24 ^{+0.09} _{-0.07}
DES15C3lpq	9.32 ^{+0.39} _{-0.20}	0.86 ^{+0.73} _{-0.53}	-8.43 ^{+0.68} _{-0.53}	8.59 ^{+0.26} _{-0.59}	-	-	-	8.59 ^{+0.26} _{-0.59}	8.25 ^{+0.25} _{-0.25}
DES15C3nat	10.49 ^{+0.58} _{-0.17}	1.14 ^{+0.98} _{-0.60}	-9.34 ^{+0.41} _{-0.43}	-	-	-	-	-	-
DES15C3mgq	8.41 ^{+0.29} _{-0.12}	-1.12 ^{+0.55} _{-0.37}	-9.53 ^{+0.26} _{-0.25}	8.33 ^{+0.25} _{-0.26}	8.29 ^{+0.51} _{-0.50}	8.38 ^{+0.17} _{-0.20}	8.29 ^{+0.11} _{-0.16}	8.37 ^{+0.46} _{-0.41}	8.28 ^{+0.21} _{-0.13}
DES15E2nqh	9.28 ^{+0.28} _{-0.22}	0.11 ^{+0.72} _{-0.72}	-9.17 ^{+0.66} _{-0.45}	8.50 ^{+0.37} _{-0.76}	-	-	-	8.50 ^{+0.37} _{-0.76}	8.20 ^{+0.32} _{-0.32}
DES15C3opk	9.89 ^{+0.22} _{-0.44}	0.89 ^{+0.67} _{-1.20}	-9.01 ^{+0.55} _{-0.75}	8.68 ^{+0.27} _{-0.78}	-	-	-	8.68 ^{+0.27} _{-0.78}	8.33 ^{+0.29} _{-0.29}
DES15C3opp	9.15 ^{+0.32} _{-0.21}	0.13 ^{+0.84} _{-0.78}	-9.02 ^{+0.72} _{-0.57}	8.59 ^{+0.19} _{-0.28}	-	-	-	8.59 ^{+0.19} _{-0.28}	8.25 ^{+0.17} _{-0.10}
DES16E2pv	9.57 ^{+0.43} _{-0.12}	0.07 ^{+0.98} _{-0.39}	-9.50 ^{+0.55} _{-0.24}	8.53 ^{+0.35} _{-0.74}	-	-	-	8.53 ^{+0.35} _{-0.74}	8.21 ^{+0.32} _{-0.32}
DES16S1bbp	9.06 ^{+0.30} _{-0.39}	0.30 ^{+0.79} _{-0.86}	-8.75 ^{+0.49} _{-0.48}	8.26 ^{+0.08} _{-0.17}	8.14 ^{+0.17} _{-0.17}	8.26 ^{+0.04} _{-0.04}	8.30 ^{+0.04} _{-0.04}	8.19 ^{+0.20} _{-0.20}	8.28 ^{+0.01} _{-0.04}
DES16X3cxn	9.55 ^{+0.57} _{-0.08}	-0.32 ^{+1.00} _{-0.19}	-9.88 ^{+0.43} _{-0.26}	8.53 ^{+0.25} _{-0.37}	-	-	-	8.53 ^{+0.25} _{-0.37}	8.21 ^{+0.21} _{-0.21}
DES16C1cbd	10.77 ^{+0.15} _{-0.15}	-1.43 ^{+0.94} _{-1.94}	-12.20 ^{+0.79} _{-1.79}	8.72 ^{+0.12} _{-0.12}	-	-	-	8.72 ^{+0.12} _{-0.12}	8.36 ^{+0.10} _{-0.10}
DES16X3ega	9.94 ^{+0.18} _{-0.06}	0.30 ^{+0.26} _{-0.21}	-9.64 ^{+0.08} _{-0.15}	8.58 ^{+0.18} _{-0.18}	8.43 ^{+0.17} _{-0.19}	8.47 ^{+0.08} _{-0.09}	8.61 ^{+0.07} _{-0.06}	8.77 ^{+0.06} _{-0.07}	8.51 ^{+0.08} _{-0.08}
DES16X3erw	9.89 ^{+0.26} _{-0.25}	0.94 ^{+0.62} _{-0.75}	-8.94 ^{+0.36} _{-0.51}	8.72 ^{+0.09} _{-0.10}	-	-	-	8.72 ^{+0.09} _{-0.10}	8.37 ^{+0.09} _{-0.09}
DES16C3gin	9.85 ^{+0.32} _{-0.27}	0.45 ^{+0.68} _{-0.68}	-9.41 ^{+0.41} _{-0.12}	8.80 ^{+0.09} _{-0.12}	-	-	-	8.80 ^{+0.09} _{-0.12}	8.44 ^{+0.12} _{-0.12}
DES16S1dxu	8.60 ^{+0.41} _{-0.28}	-0.49 ^{+0.70} _{-0.71}	-9.09 ^{+0.29} _{-0.43}	8.27 ^{+0.19} _{-0.21}	8.25 ^{+0.43} _{-0.50}	8.22 ^{+0.12} _{-0.16}	8.26 ^{+0.09} _{-0.14}	8.37 ^{+0.20} _{-0.21}	8.21 ^{+0.10} _{-0.14}
DES16X1eho	10.70 ^{+0.42} _{-0.24}	0.01 ^{+1.33} _{-0.50}	-10.69 ^{+0.91} _{-0.26}	-	-	-	-	-	-
DES17C3gop	9.90 ^{+0.09} _{-0.09}	0.19 ^{+0.38} _{-0.38}	-9.71 ^{+0.28} _{-0.48}	8.61 ^{+0.34} _{-0.58}	-	-	-	8.61 ^{+0.34} _{-0.58}	8.27 ^{+0.34} _{-0.34}
DES17S2fee	11.20 ^{+0.22} _{-0.14}	0.22 ^{+0.70} _{-1.91}	-10.92 ^{+0.48} _{-1.77}	8.59 ^{+0.21} _{-0.22}	8.39 ^{+0.05} _{-0.05}	8.78 ^{+0.04} _{-0.04}	-	-	8.86 ^{+0.05} _{-0.05}
DES17X3dxu	10.49 ^{+0.22} _{-0.32}	1.02 ^{+0.63} _{-0.69}	-9.47 ^{+0.40} _{-0.52}	-	-	-	-	-	-
DES17X3cds	9.36 ^{+0.12} _{-0.12}	-0.18 ^{+0.83} _{-0.25}	-9.53 ^{+0.13} _{-0.13}	8.76 ^{+0.20} _{-0.33}	-	-	-	8.76 ^{+0.20} _{-0.33}	8.41 ^{+0.22} _{-0.24}
DES17X3hxi	8.60 ^{+0.00} _{-0.11}	-0.37 ^{+0.10} _{-0.11}	-8.96 ^{+0.10} _{-0.00}	8.55 ^{+0.36} _{-0.82}	-	-	-	8.55 ^{+0.36} _{-0.82}	8.22 ^{+0.34} _{-0.34}
DES13E2lpk	10.66 ^{+0.10} _{-0.09}	0.46 ^{+0.45} _{-0.36}	-10.20 ^{+0.35} _{-0.15}	8.92 ^{+0.03} _{-0.03}	-	-	-	8.92 ^{+0.03} _{-0.03}	8.58 ^{+0.03} _{-0.03}
DES15C2eal	8.42 ^{+0.18} _{-0.09}	-1.22 ^{+0.33} _{-0.30}	-9.72 ^{+0.21} _{-0.21}	8.23 ^{+0.35} _{-0.35}	7.97 ^{+0.29} _{-0.51}	8.29 ^{+0.15} _{-0.18}	8.34 ^{+0.15} _{-0.20}	8.52 ^{+0.30} _{-0.49}	8.28 ^{+0.17} _{-0.17}
DES16C2ggt	9.86 ^{+0.36} _{-0.29}	0.13 ^{+0.94} _{-0.46}	-9.73 ^{+0.59} _{-0.18}	8.53 ^{+0.15} _{-0.15}	8.37 ^{+0.04} _{-0.04}	8.51 ^{+0.02} _{-0.02}	8.54 ^{+0.01} _{-0.01}	8.93 ^{+0.02} _{-0.02}	8.56 ^{+0.02} _{-0.02}
DES17C2hno	9.56 ^{+0.16} _{-0.21}	-0.02 ^{+0.33} _{-0.44}	-9.58 ^{+0.17} _{-0.24}	8.94 ^{+0.09} _{-0.17}	-	-	-	8.94 ^{+0.09} _{-0.17}	8.60 ^{+0.11} _{-0.19}

^a Linear combination of the likelihoods for D16, PP04 N2, PP04 O3N2, KK04 R23.^b Weighted average of PP04 N2, PP04 O3N2, and KK04 R23, where N2 and R23 were converted to PP04 O3N2 via Kewley & Ellison (2008).

diagram, and we find no evidence AGN amongst the 12 hosts in those diagrams either.

Due to the low S/N of the spectra in this sample, we are constrained to a subset of metallicity diagnostics by the availability of only a handful of the strongest emission lines, namely $H\alpha$, $H\beta$, $[\text{OIII}]3727$, $[\text{OIII}]4959/5007$, $[\text{NII}]6548/6583$, and $[\text{SII}]6717/6731$. Furthermore, for each host galaxy only a subset of these lines are detected - for example, $H\alpha$, $[\text{NII}]$ and $[\text{SII}]$ are redshifted out of the spectral coverage at $z > 0.3$, leaving only the oxygen and $H\beta$ lines available, mandating the use of the R23 diagnostic. For hosts at $z < 0.3$ we are able to use the $[\text{OIII}]/[\text{NII}]$ (O3N2), $[\text{NII}]/H\alpha$ (N2), and $[\text{SII}]/[\text{NII}]$ (S2N2) line ratios.

Due to the redshift range of our sample, and the limited wavelength coverage of the spectra (3000 – 8000 Å), we are unable to

use a single line ratio to estimate the oxygen abundances. We thus determine a set of indicators for which to calculate abundances. For the O3N2 and N2 indicators we use the calibration of Pettini & Pagel (2004) (PP04), and if $[\text{SII}]$ is detected we derive an abundance using the S2N2 diagnostic of Dopita et al. (2016). For the R23 indicator, we use the calibration of Kobulnicky & Kewley (2004) (KK04). At abundances around $12 + \log(\text{O}/\text{H}) \sim 8.4$, the R23 indicator becomes two-tailed, with a low and a high value of metallicity corresponding to a single R23 ratio. In cases where the lines are available, we break this degeneracy by cross-calibrating with the $[\text{NII}]/[\text{OIII}]$ ratio (Kewley & Ellison 2008). In the cases where $[\text{NII}]$ is not available, and there are no other diagnostics that can be used to inform the choice of branch, we use the host galaxy stellar mass to derive a crude metallicity estimate from the mass-

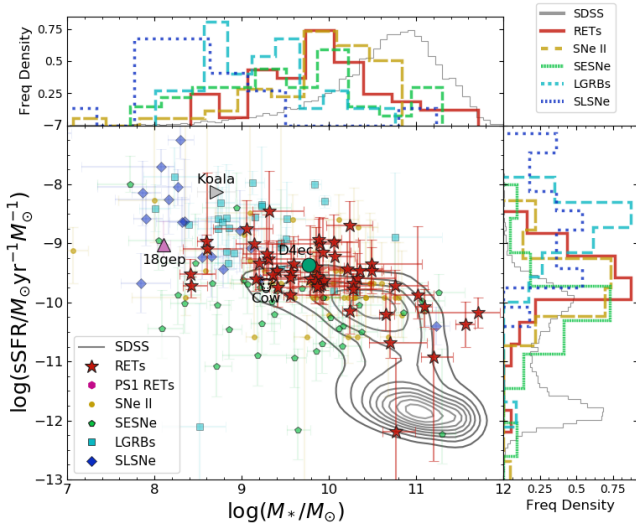


Figure 7. The sSFR of RET hosts, compared to CCSNe and the low- z SDSS sample.

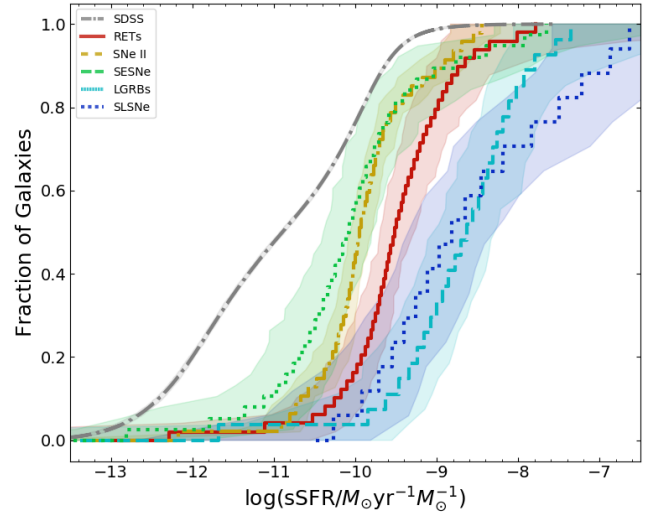


Figure 8. Cumulative distributions of the sSFR of RET hosts, compared to CCSNe and the low- z SDSS sample.

metallicity relation (MZR) of Kewley & Ellison (2008) based upon the PP04 O3N2 diagnostic. For $12 + \log(\text{O}/\text{H})_{\text{MZR}} < 8.4$ we chose the lower branch, while for higher MZR metallicities we choose the upper branch. We note that this is a rough estimation. If we leave the branch choice for those with no [NII] to be random, we find that the results are consistent to within uncertainties

The samples to which we compare metallicities span different redshift ranges, were observed with different equipment, and in many cases were compiled before certain (particularly the D16) diagnostics were devised. Therefore, in order to compare oxygen abundances between different samples we transform all abundances onto the PP04 O3N2 scale using the conversion from Kewley & Ellison (2008). This is not possible for the D16 diagnostic, so we discard it from the rest of our analysis, although for completeness we provide it for DES RET hosts where available. For samples that quoted multiple diagnostics, or for which sufficient line flux measurements were provided from which to calculate multiple diagnostics, we transform them all to the PP04 O3N2 scale. Following the prescription of Krühler et al. (2015) we simultaneously minimise the oxygen abundance against the probability density functions (PDFs) of the various different diagnostics scaled to PP04 O3N2, resulting in a final ‘best’ PDF. We take 1σ uncertainties from the 16th and 84th percentiles of these PDFs, and for DES RETs display the results in Table 2.

5 ANALYSIS

5.1 Star formation rate

Fig. 6 shows the ‘star formation main sequence’ (SFMS) of RET host galaxies, as determined from photometric SED fitting along with that for the comparison samples and for the field galaxies of SDSS. RETs follow CCSNe, LGRBs and SLSNe in systematically avoiding passive galaxies, evidence that RETs require the presence of star-formation and thus are linked to massive stars. The local rapid transients Cow, Koala and SN2018gep are lower in mass than the majority of RETs. SN2018gep and Cow lie along the SFMS, while Koala sits in the starburst regime, which is not heavily populated by DES RETs.

Fig. 7 is similar to Fig. 6, except that here SFR has been normalised by stellar mass, and thus shows the specific star-formation rate (sSFR), which is more representative measure of the star-forming efficiency. It is once again clear that RET hosts lie systematically above the majority of SDSS star-forming galaxies. Normalised by mass, it is here perhaps clearer to see that RET hosts lie at higher sSFR than CCSNe hosts, but not in the extremely star-forming environments home to LGRBs or SLSNe.

We show the cumulative distribution of sSFR in Fig. 8. The RET hosts are clearly shifted to higher sSFRs than CCSNe. To statistically compare the host sSFR distribution of RETs with the other samples, we employ the method of Wiseman et al. (2020). For each pair of samples, we model the PDFs as skewed normal distributions described by the parameters ‘loc’ (location, identical to mean for zero skewness), ‘scale’ (spread, identical to standard deviation for zero skewness)², and ‘skewness’. To impose priors on loc and scale, we combine the two samples and use normal priors centered on the combined mean and twice the combined standard deviation respectively, while for skewness the prior is a broad normal distribution centered on 0. We note that the loc parameter describes the location of the distribution (its relative position on the x-axis) and is not a mean, median, or mode. A highly-skewed distribution may have a loc that lies above almost the entire sample. A worked example as well as the results from the simultaneous fitting are displayed in Appendix B.

The comparison shows RET hosts to be shifted to higher sSFRs than CCSNe. In 100% of the posterior samples the RETs were located at higher average sSFRs than SNe II, while the same was true 76% of the time for RETs when comparing with SESNe. RET host galaxies are significantly lower in sSFR than LGRBs. While the distributions are similar in shape, with a mean difference in scale of 0.28, the mean difference in loc is -1.64, with no overlap between the posterior distributions. The sSFR distribution of SLSNe hosts is heavily positively skewed (with alpha values of $5.54^{+1.8}_{-0.98}$

² See Wiseman et al. (2020) for a detailed description of the fitting procedure and the parameters describing the skewed normal distributions

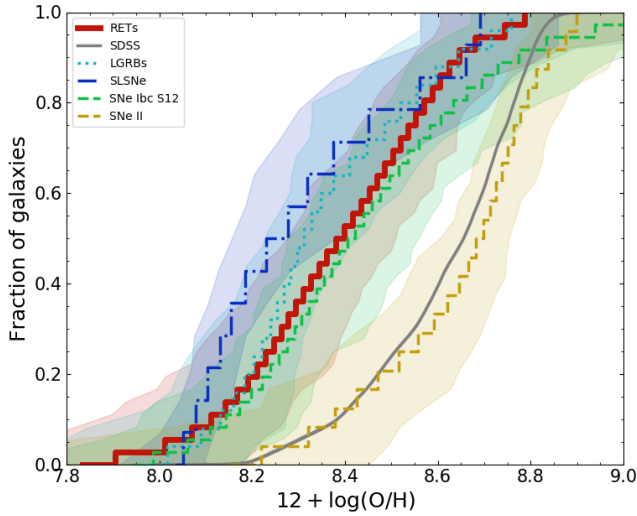


Figure 9. Cumulative distributions of the gas-phase oxygen abundances of RET hosts, compared to CCSNe and the low- z SDSS sample.

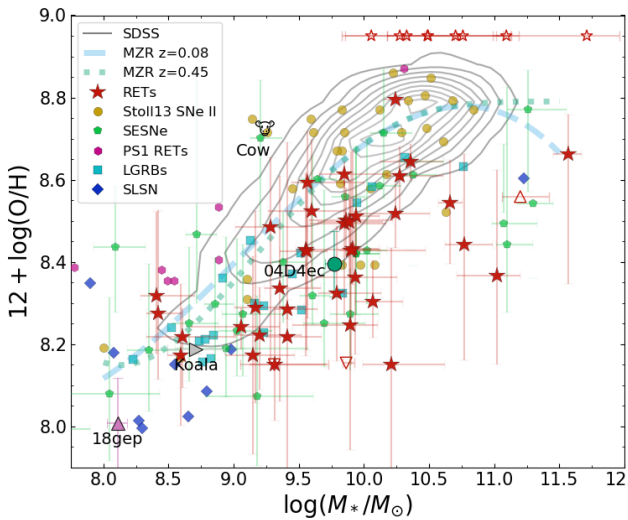


Figure 10. The mass-metallicity relation (MZR) for RET host galaxies. Upward- and downward-pointing triangles reflect lower and upper limits respectively. The DES RETs with no metallicity measurement have been placed at the top of the figure for completeness.

compared to $-0.18^{+0.75}_{-0.76}$ for RET hosts). The strong high-sSFR tail shows SLSNe occur in a different galaxy population to RETs.

5.2 Metallicity

In the Section 5.1 we demonstrate that RETs occur in galaxies with systematically higher sSFR than CCSNe, to which one explanation is that they are related to more massive stars. A further property that could directly impact the composition of stellar populations harbouring potential RET progenitors is the metallicity. Using the gas-phase oxygen abundances calculated in Section 4.3 as a proxy for metallicity, we can compare the chemical state of RET host galaxies with CCSNe and star-forming field galaxies. The cumulative distributions of metallicity are displayed in Fig. 9, and show

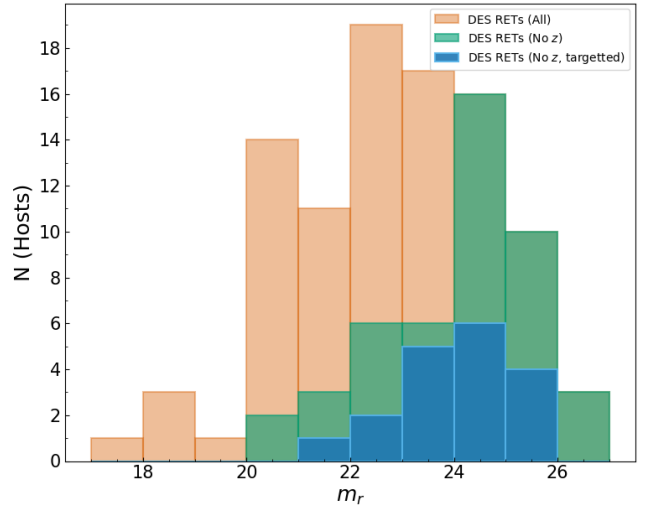


Figure 11. Observer-frame r -band magnitude distribution for the host galaxies of RETs in DES. The orange histogram represents the 96/106 DES RETs for which a host was detected. The green histogram shows those that did not have a successful redshift measurement, while blue shows those with no redshift despite being targeted by OzDES.

RET hosts to be inconsistent with SNe II and field galaxies. The RET curve lies at lower metallicity than those galaxies, and appears visually similar to the curves for SESNe. The metallicity distribution of SESNe is, however, quite broad (e.g. Anderson et al. 2010), with different subclasses showing different trends (with SNe Ic host environments exhibiting higher metallicity than Ib, and IIb much lower). RETs occur, on average, in slightly more metal-rich environments than LGRBs and SLSNe.

We compare the metallicity distributions in the same way as the sSFRs. The RET host metallicity distribution shows a broad peak, leading to two families of skewed-Gaussians that fit it well, one with a low-valued centre ($12 + \log(O/H) \sim 8.1$) and a positive skew, and the other with a higher-valued centre ($12 + \log(O/H) \sim 8.6$). Comparing the DES RETs to the Stoll et al. (2013) SNe II shows the latter to be centred around 8.8, with the centre being greater than the RETs in 94% of samples. We determine that the RET host metallicities are derived from a different population to the SNe II. On the other hand, simultaneous fits with SESNe show very similar distributions, including a smaller higher-metallicity peak, such that they are indistinguishable statistically.

The median CDFs of LGRBs and SLSNe show divergence from the RETs, particularly at low metallicity. As a result, the locs of their fits are shifted compared to the RETs. In 67% of samples, the RET sample had a higher loc than the LGRBs, with RETs also showing a broader distribution 67% of the time. While these effects are not as significant as with the RETs - SNe II comparison, there is mild evidence that RETs located in galaxies with higher metal content than LGRBs. The effect is more pronounced for SLSNe, where the RETs have a higher metallicity for the distribution peak 92% of the time. The SLSN distribution is also more strongly skewed, with 89% of the posterior distribution being more strongly skewed than the RETs. There is thus mild-to-strong evidence that RETs occur in more metal-rich environments than SLSNe.

In Fig. 10 we show the MZR for the RET and comparison samples. The contours show the MZR for low-redshift ($z = 0.08$) star-forming galaxies from SDSS, adjusted to the PP04 O3N2 di-

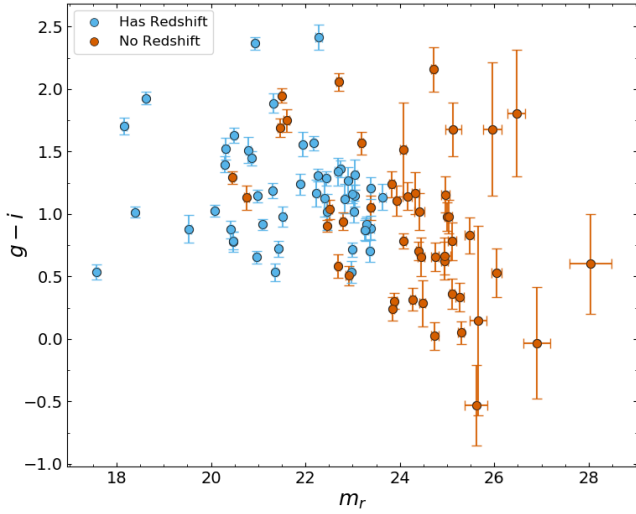


Figure 12. The colour-magnitude distribution of RET hosts with (cyan) and without (orange) redshifts. There is an excess of objects with blue colours that do not have redshift measurements.

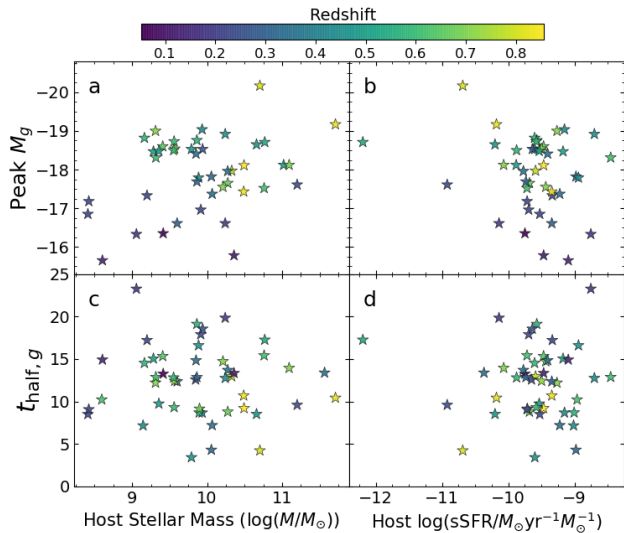


Figure 13. RET lightcurve properties as a function of host galaxy measurements.

Cut	Number of remaining objects
All RETs	106
No redshift	48
Host in SN Deep	40
Host in SVA1	34
Targetted by OzDES	18

Table 3. Numbers of RETs passing various cuts relating to redshift targeting.

6 DISCUSSION

6.1 Selection Biases

The properties presented in Section 5 are derived from a subset of the total sample of RETs. Of 106 objects, under half (52/106) have secure host galaxy redshifts. Three of these were obtained from transient spectra, for which we are unable to disentangle the host and transient contributions, and four were obtained by programmes for which we do not have access to the spectra. Of the remaining 45, it was possible to derive a metallicity or at least a limit for 40 host galaxies, while five exceeded the redshift range for the necessary lines to fall within the wavelength coverage of AAOmega. The observed metallicity distribution could have arisen if the galaxies without redshifts (and metallicities) are systematically higher in metallicity than those for which measurements were possible. For low SNR objects, redshifts are typically obtained from only two of the strongest lines (e.g. H α , H β , [OIII], and [OII]). It is likely that the redshifts were not obtained because the galaxies are physically smaller or are at higher redshift. However, galaxies with high metallicity have weaker [OIII] lines, meaning they are less likely to have a positive redshift detection compared to less enriched galaxies with the same mass and redshift. Future, deeper spectral observation programmes as well as large, complete low-redshift samples are necessary to eliminate this possible bias.

Another possibility is that the hosts without a redshift are mostly non-starforming, passive galaxies, for which a redshift is typically harder to obtain than for emission-line galaxies (Yuan et al. 2015; Childress et al. 2017; Lidman et al. 2020). In order to test this possibility, we examined the RETs that do not have a host galaxy redshift. Table 3 shows the numbers of RETs that failed various stages of the redshifting process, and is summarised in Fig. 11. Of the 48 objects without a redshift, 40 of them have host galaxies detected in the SN Deep coadds of Wiseman et al. (2020). Of more significance is that only 34 have host galaxies in the SVA1 catalogues which were used for targeting during the OzDES campaign. The other, ‘hostless’, objects are either transients that are located remotely from a galaxy that was detected, or are hosted by a galaxy that was not detected. Non-detected hosts are either intrinsically faint and thus low in mass, situated at high redshift, or both. Neither are expected to be systematically higher in metallicity than the detected hosts. Similarly, a further 16 hosts were detected but not targetted by OzDES, due to being too faint to pass the selection criteria ($m_r < 24.5$), leaving 18 that were targetted but no redshift was found. The resulting redshift completeness of targetted objects is 70% (82% for objects brighter than $m_r = 24$ mag, which is in line with the average for OzDES as a whole (Lidman et al. 2020). In Fig. 12 we show the observer-frame r -band magnitudes and $g-i$ colours for all RET hosts that were detected. The 40 objects with detected hosts but no redshift lie at fainter magnitudes, and appear to extend to bluer colours than those with secure redshifts. This is contrary to the hypothesis that they are high-redshift and/or passive hosts, but instead are low-mass, star-forming galaxies whose line fluxes were not strong enough to be detected.

agnostic. We use the MZR parameterisation Zahid et al. (2014) to show the best fit to the MZR for star-forming galaxies. The blue dashed line shows the fit to the low- z data, while the green dashed line corresponds to the MZR at $z = 0.45$, the mean redshift of the RET host sample. The RET hosts lie systematically below the galaxy MZR fits as well as the bulk of the SDSS galaxies, meaning that for a given stellar mass they have a lower metallicity. They populate similar regions to SESNe, LGRBs and SLSNe but are clearly offset from the SNe II.

6.2 Origin of RETs

The sample of DES RETs shows a preference for low-metallicity, strongly star-forming host environments. The PDF of their metallicities displays a strong similarity to the hosts of SNe Ibc, as well as LGRBs. There is a clear difference to the PDFs of SNe II, which follow SDSS field galaxies. The preference for low-metallicity systems is not as strong as for LGRBs or SLSNe, but the highest metallicities found in all three samples are very similar at around solar metallicity. This result is further suggestive of a stripped-envelope, massive-star origin for RETs. The population of RET hosts lies, on average, between CCSNe and LGRBs/SLSNe in terms of both star formation and metallicity. A loose correlation exists between the luminosity and rarity of events, and the host galaxy conditions required for their formation. The rough rate of RETs ($\geq 10^{-6} \text{Mpc}^{-3} \text{yr}^{-1}$), Drout et al. 2014, P18, Tampo et al. 2020) is $\sim 1\%$ of the CCSN rate (Li et al. 2011; Horiuchi et al. 2011; Strolger et al. 2015), which itself is divided into the more common SNe II and subdominant SESNe (Kelly & Kirshner 2012; Frohmaier et al. 2020). At $\sim 1\%$ of the CCSN rate, RETs are more common than SLSNe ($\sim 0.01 - 0.05\%$ of CCSNe; McCrum et al. 2015; Prajs et al. 2017; Frohmaier et al. 2020) and LGRBs (intrinsically $\sim 0.08\%$ when accounting for beaming; Graham & Schady 2016). These figures place the DES RETs between extreme objects (SLSNe, LGRBs) and more common SNe (SNe II, SESNe) in terms of rate, matching their location in host galaxy parameter space. While stressing that these associations are loose - rates are uncertain and host galaxy parameters span wide ranges for all transients - they are both linked to the respective transients' progenitor channels. Based upon both indicators, it is reasonable to infer that RETs are linked to very massive stars, *potentially stripped of their envelopes, and possibly sharing some of the extreme properties of SLSNe or LGRBs*. It could therefore be possible that RETs are an intermediate and/or precursory step, whereby the initial collapse of the star occurs leading to a shocked photosphere, but conditions are not highly tuned enough for a LGRB or SLSN and the respective central engine does not form.

6.3 Correlations between lightcurve and host galaxy properties

Many classes of transients show trends between properties intrinsic to the objects themselves and their host galaxies. For example, SNe Ia lightcurves appear to be broader in less massive galaxies with higher sSFRs (Sullivan et al. 2006; Neill et al. 2009; Howell et al. 2009; Sullivan et al. 2010; Roman et al. 2018; Kelsey 2020), while SLSNe that have been fit with a magnetar model show a tentative relationship between the magnetar spin period and host galaxy metallicity (Chen et al. 2016). In Fig. 13 we show the RET peak magnitude (upper panels) and decline rate parameterised as t_{half} , the time taken for the LC to decline to half the peak brightness (lower panels) and how they correspond to host galaxy stellar mass (left-hand panels) and sSFR (right-hand panels). The decline rates have been converted to the rest-frame of the transients, while the peak magnitudes have been k-corrected assuming a simple black-body SED. There is no correlation between decline rate and either stellar mass or sSFR, while there are hints of a trend between peak magnitude and both mass and sSFR. These apparent trends are driven by the more extreme hosts (the three with $\log(M_*/M_\odot) < 9$ and one with very high mass/low sSFR). Assuming that these points are not outliers, the trends are still likely driven by selection effects. At higher redshifts, only the brighter transients are recovered by

the survey and our selection method, while at those redshifts only the more massive galaxies are detected. This effect can be seen in panel a) of Fig. 13, with redshift increasing from the lower left to the upper right, while the same is true from the upper left to lower right in panel b. It is hoped that a complete, volume-limited sample of RETs will be obtained by The Rubin Observatory Legacy Survey of Space and Time (LSST) allowing the removal of these biases in order to reveal any underlying relationships.

6.4 Comparison with local RETs

The nearby transient AT2018cow has drawn many comparisons to the cosmological RETs from DES and PS1 (e.g. Perley et al. 2019; Margutti et al. 2019; Fox & Smith 2019; Mohan et al. 2020) due to its rapid evolution and blue colour. AT2018cow displayed a contracting photosphere as well as evidence for central-engine power alongside an unusual spectrum that showed similarities to broad-lined SNe Ic (SN Ic-bl) at early stages (e.g. Xu et al. 2018; Izzo et al. 2018), developing to something entirely different later on (Perley et al. 2019) with hints of similarities to interacting SNe Ibn (Fox & Smith 2019). There have been several suggestions that AT2018cow is indeed an analogue of the high- z RETs. The host galaxy of AT2018cow appears to be moderately star forming and lies very close to the centre of the SFMS (Figs. 6,7), along with many of the DES RET hosts. However, the host lies significantly above the fiducial MZR in Fig. 10, suggesting that it has an abnormally high metallicity for its stellar mass. This is in contrast to the DES RET hosts, which are systematically less enriched for a given stellar mass.

Other local rapid transients include SN2018gep (Ho et al. 2019), a spectroscopically classified SN Ic-bl with a rapid rise. The host of SN2018gep appears more similar to the DES RET sample, lying in the same M_* -SFR and M_* -sSFR plane, as well as lying below the MZR. While the SN2018gep host is lower in stellar mass than any DES RET ($\log(M/M_\odot) = 8.11$, galaxies of that mass are unlikely to have been detected at the redshifts of the DES RETs (Wiseman et al. 2020). The authors' conclusion that SN2018gep is related to a shock-breakout of a massive, stripped-envelope star is similar to that posited in Section 6.2.

The rapidly evolving lightcurve of ZTF18abvkwla ("the Koala") has been attributed to shock interaction, while radio emission can be explained by a collimated jet. The host of the Koala is a low metallicity starburst more typical of LGRBs and SLSNe, and places this transient at the very extreme end of the DES RET host population. While we note that the Ho et al. (2020) study made multiple non-detections of radio emission from the DES RETs, these were taken at very late epochs (≥ 1 year), so the presence of jets in the early evolution is not ruled out. Seen from the other point of view, we cannot rule out that the Koala comes from the same population of transients as the DES RETs.

SN2018kzr (McBrien et al. 2019) is one of the most rapidly declining transients ever discovered, with spectral signatures similar to SNe Ic. While host galaxy properties are not derived, the authors of that paper refer to narrow emission from the host galaxy, along with an apparently small, blue, star-forming host and is thus consistent with the DES RETs.

7 CONCLUSIONS

By analysing the host galaxies of 49 rapidly evolving transients (RETs) discovered in the Dark Energy Survey, we have been able

to place constraints on the nature of this as-yet unexplained phenomenon. We conclude that RETs are strongly linked to massive stars, due to their apparent reliance on star formation. Their origin is likely from more massive stars than SNe II, as they require higher sSFR. RET hosts are lower in metallicity than SNe II hosts, suggesting some reliance on rotational energy or other metallicity-dependent effects. Of the RET analogues discovered in the local Universe, ZTF18abvkwla shares the most similar host galaxy characteristics with the DES RET population. SN2018gep appears in a galaxy too faint to have been detected by DES-SN at the redshift of most of the DES RETs, while the host of AT2018cow is much higher in metallicity.

While current surveys such as ZTF, GOTO, and BlackGEM are well equipped to find low-redshift RETs, a sample similar to that presented here will likely not be collected until LSST comes online. With several hundreds of objects, detailed studies of RETs and their hosts will be possible in a systematic and more complete manner as has been achieved with LGRBs and SLSNe. At that point, the conclusions of this paper will be able to be tested.

ACKNOWLEDGEMENTS

We acknowledge support from STFC grant ST/R000506/1. L.K. was supported by the Science and Technology Facilities Council (grant number ST/P006760/1) through the DISCnet Centre for Doctoral Training. M.S. and M.S. acknowledge support from EU/FP7-ERC grant 615929. L.G. was funded by the European Union's Horizon 2020 research and innovation programme under the Marie Skłodowska-Curie grant agreement No. 839090.

This paper makes use of observations taken using the Anglo-Australian Telescope under programs ATAC A/2013B/12 and NOAO 2013B-0317.

This research used resources of the National Energy Research Scientific Computing Center (NERSC), a U.S. Department of Energy Office of Science User Facility operated under Contract No. DE-AC02-05CH11231.

Funding for the DES Projects has been provided by the U.S. Department of Energy, the U.S. National Science Foundation, the Ministry of Science and Education of Spain, the Science and Technology Facilities Council of the United Kingdom, the Higher Education Funding Council for England, the National Center for Supercomputing Applications at the University of Illinois at Urbana-Champaign, the Kavli Institute of Cosmological Physics at the University of Chicago, the Center for Cosmology and Astro-Particle Physics at the Ohio State University, the Mitchell Institute for Fundamental Physics and Astronomy at Texas A&M University, Financiadora de Estudos e Projetos, Fundação Carlos Chagas Filho de Amparo à Pesquisa do Estado do Rio de Janeiro, Conselho Nacional de Desenvolvimento Científico e Tecnológico and the Ministério da Ciência, Tecnologia e Inovação, the Deutsche Forschungsgemeinschaft and the Collaborating Institutions in the Dark Energy Survey.

The Collaborating Institutions are Argonne National Laboratory, the University of California at Santa Cruz, the University of Cambridge, Centro de Investigaciones Energéticas, Medioambientales y Tecnológicas-Madrid, the University of Chicago, University College London, the DES-Brazil Consortium, the University of Edinburgh, the Eidgenössische Technische Hochschule (ETH) Zürich, Fermi National Accelerator Laboratory, the University of Illinois at Urbana-Champaign, the Institut de Ciències de l'Espai (IEEC/CSIC), the Institut de Física d'Altes Energies, Lawrence Berkeley National Laboratory, the Ludwig-Maximilians Universität

München and the associated Excellence Cluster Universe, the University of Michigan, the National Optical Astronomy Observatory, the University of Nottingham, The Ohio State University, the University of Pennsylvania, the University of Portsmouth, SLAC National Accelerator Laboratory, Stanford University, the University of Sussex, Texas A&M University, and the OzDES Membership Consortium.

Based in part on observations at Cerro Tololo Inter-American Observatory, National Optical Astronomy Observatory, which is operated by the Association of Universities for Research in Astronomy (AURA) under a cooperative agreement with the National Science Foundation.

The DES data management system is supported by the National Science Foundation under Grant Numbers AST-1138766 and AST-1536171. The DES participants from Spanish institutions are partially supported by MINECO under grants AYA2015-71825, ESP2015-66861, FPA2015-68048, SEV-2016-0588, SEV-2016-0597, and MDM-2015-0509, some of which include ERDF funds from the European Union. IFAE is partially funded by the CERCA program of the Generalitat de Catalunya. Research leading to these results has received funding from the European Research Council under the European Union's Seventh Framework Program (FP7/2007-2013) including ERC grant agreements 240672, 291329, and 306478. We acknowledge support from the Brazilian Instituto Nacional de Ciência e Tecnologia (INCT) e-Universe (CNPq grant 465376/2014-2).

This manuscript has been authored by Fermi Research Alliance, LLC under Contract No. DE-AC02-07CH11359 with the U.S. Department of Energy, Office of Science, Office of High Energy Physics.

This work makes extensive use of Astropy,³ a community-developed core Python package for Astronomy (Astropy Collaboration et al. 2013, 2018), Pandas (McKinney 2010), and matplotlib (Hunter 2007).

REFERENCES

- Ahumada R., et al., 2019
- Anderson J. P., Covarrubias R. A., James P. A., Hamuy M., Habergham S. M., 2010, *MNRAS*, 407, 2660
- Angus C. R., Levan A. J., Perley D. A., Tanvir N. R., Lyman J. D., Stanway E. R., Fruchter A. S., 2016, *MNRAS*, 458, 84
- Angus C. R., et al., 2019, *MNRAS*, 487, 2215
- Arcavi I., et al., 2016, *ApJ*, 819, 35
- Astropy Collaboration et al., 2013, *A&A*, 558
- Astropy Collaboration et al., 2018, *ApJ*, 156, 123
- Baldry I. K., et al., 2018, *MNRAS*, 474, 3875
- Baldwin J. A., Phillips M. M., Terlevich R., 1981, *PASP*, 93, 5
- Bruzual G., Charlot S., 2003, *MNRAS*, 344, 1000
- Cappellari M., 2017, *MNRAS*, 466, 798
- Cappellari M., Emsellem E., 2004, *PASP*, 116, 138
- Cappellari M., Michele 2012, ascl, p. ascl:1210.002
- Cardelli J. A., Clayton G. C., Mathis J. S., 1989, *ApJ*, 345, 245
- Chabrier G., 2003, *PASP*, 115, 763
- Chen T. W., Smartt S. J., Yates R. M., Nicholl M., Krühler T., Schady P., Dennefeld M., Inserra C., 2016, *MNRAS*, 470, 3566
- Childress M., et al., 2013, *ApJ*, 770, 107
- Childress M. J., et al., 2017, *MNRAS*, 472, 273
- Croom S., Saunders W., Heald R., 2004, *AAONw*, 106, 12
- De Cia A., et al., 2018, *ApJ*, 860, 100

³ <http://www.astropy.org>

- Dopita M. A., Kewley L. J., Sutherland R. S., Nicholls D. C., 2016, *Ap&SS*, 361, 61
- Driver S. P., et al., 2009, *Astronomy and Geophysics*, 50, 12
- Drout M. R., et al., 2014, *ApJ*, 794, 23
- Foreman-Mackey D., 2016, *The Journal of Open Source Software*, 1, 24
- Fox O. D., Smith N., 2019, *MNRAS*, 488, 3772
- Frohmaier C., Angus C. R., Sullivan M., 2020, *MNRAS*, in prep
- Fruchter A. S., et al., 2006, *Nature*, 441, 463
- Gal-Yam A., 2012, *Science*, 337, 927
- Galama T. J., et al., 1998, *Nature*, 395, 670
- Galbany L., et al., 2018, *ApJ*, 855, 107
- Gallazzi A., Bell E. F., 2009, *Astrophysical Journal, Supplement Series*, 185, 253
- Gallazzi A., Charlot S., Brinchmann J., White S. D., Tremonti C. A., 2005, *MNRAS*, 362, 41
- Graham J. F., Schady P., 2016, *ApJ*, 823, 154
- Hjorth J., et al., 2003, *Nature*, 423, 847
- Ho A. Y. Q., et al., 2019, *ApJ*, 871, 73
- Ho A. Y. Q., et al., 2020
- Hoffman M. D., Gelman A., 2014, *Journal of Machine Learning Research*, 15, 1593
- Horiuchi S., Beacom J. F., Kochanek C. S., Prieto J. L., Stanek K. Z., Thompson T. A., 2011, *ApJ*, 738, 154
- Howell D. A., et al., 2009, *ApJ*, 691, 661
- Hunter J. D., 2007, *Computing in Science and Engineering*, 9, 99
- Iglesias-Páramo J., et al., 2013, *A&A*, 553, L7
- Iglesias-Páramo J., et al., 2016, *ApJ*, 826, 71
- Izzo L., et al., 2018, *ATel*, 11753, 1
- James P. A., Anderson J. P., 2006, *A&A*, 453, 57
- Japelj J., et al., 2016, *A&A*, 590, A129
- Kauffmann G., et al., 2003, *MNRAS*, 341, 33
- Kelly P. L., Kirshner R. P., 2012, *ApJ*, 759, 107
- Kelly P. L., Kirshner R. P., Pahre M., 2008, *ApJ*, 687, 1201
- Kelsey L., 2020, *MNRAS*, in prep
- Kewley L. J., Ellison S. L., 2008, *ApJ*, 681, 1183
- Kewley L. J., Dopita M. A., Leitherer C., Davé R., Yuan T., Allen M., Groves B., Sutherland R., 2013, *ApJ*, 774, 100
- Klebesadel R. W., Strong I. B., Olson R. A., 1973, *ApJ*, 182, L85
- Kobulnicky H. A., Kewley L. J., 2004, *ApJ*, 617, 240
- Krühler T., et al., 2015, *A&A*, 581, A125
- Kuin N. P. M., et al., 2019, *MNRAS*, 487, 2505
- Le Floc'h E., Charmandaris V., Forrest W. J., Mirabel I. F., Armus L., Devost D., 2006, *ApJ*, 642, 636
- Leloudas G., et al., 2015, *MNRAS*, 449, 917
- Levesque E. M., Kewley L. J., Graham J. F., Fruchter A. S., 2010, *ApJ*, 712
- Li W., Chornock R., Leaman J., Filippenko A. V., Poznanski D., Wang X., Ganeshalingam M., Mannucci F., 2011, *MNRAS*, 412, 1473
- Lidman C., Tucker B. E., Davis T. M., Uddin S. A., Others A., 2020, *MNRAS*, in prep
- Lunnan R., et al., 2014, *ApJ*, 787, 138
- Lunnan R., et al., 2018, *ApJ*, 852, 81
- Lytikov M., Toonen S., 2019, *MNRAS*, 487, 5618
- Margutti R., et al., 2019, *ApJ*, 872, 18
- McBrien O. R., et al., 2019, *J 10.3847/2041-8213/ab4dae*
- McCrum M., et al., 2015, *MNRAS*, 448, 1206
- McKinney W., 2010, Technical report, Data Structures for Statistical Computing in Python
- Modjaz M., et al., 2008, *ApJ*, 135, 1136
- Mohan P., An T., Yang J., 2020, *ApJ*, 888, L24
- Morokuma-Matsui K., et al., 2019, *ApJ*, 879, L13
- Neill J. D., et al., 2009, *ApJ*, 707, 1449
- Neill J. D., et al., 2011, *ApJ*, 727, 15
- Palmerio J. T., et al., 2019, *A&A*, 623, A26
- Perley D. A., et al., 2016a, *ApJ*, 817, 8
- Perley D. A., et al., 2016b, *ApJ*, 830, 13
- Perley D. A., et al., 2019, *MNRAS*, 484, 1031
- Pettini M., Pagel B. E. J., 2004, *MNRAS*, 348, L59
- Prajs S., et al., 2017, *MNRAS*, 464, 3568
- Prentice S. J., et al., 2018, *ApJ*, 865, L3
- Pursiainen M., et al., 2018, *MNRAS*, 481, 894
- Pursiainen M., et al., 2019
- Quimby R. M., et al., 2011, *Nature*, 474, 487
- Rest A., et al., 2018, *Nat. Astron.*, 2, 307
- Roman M., et al., 2018, *A&A*, 615, A68
- Sako M., et al., 2008, *ApJ*, 135, 348
- Salpeter E. E., 1955, *ApJ*, 121, 161
- Sanders N. E., et al., 2012, A spectroscopic study of type Ibc supernova host galaxies from untargated surveys ([arXiv:1206.2643](https://arxiv.org/abs/1206.2643)), [doi:10.1088/0004-637X/758/2/132](https://doi.org/10.1088/0004-637X/758/2/132)
- Schlegel D. J., Finkbeiner D. P., Davis M., 1998, *ApJ*, 500, 525
- Schulze S., et al., 2018, *MNRAS*, 473, 1258
- Soker N., Grichener A., Gilkis A., 2019, *MNRAS*, 484, 4972
- Speagle J. S., Steinhardt C. L., Capak P. L., Silverman J. D., 2014, *Astrophysical Journal, Supplement Series*, 214, [arXiv:2003.02669](https://arxiv.org/abs/2003.02669)
- Stanek K. Z., et al., 2006, *Acta Astronomica*, 56, 333
- Stoll R., Prieto J. L., Stanek K. Z., Pogge R. W., 2013, *ApJ*, 773, 12
- Strolger L.-G., et al., 2015, *ApJ*, 813, 93
- Sullivan M., et al., 2006, *ApJ*, 648, 868
- Sullivan M., et al., 2010, *MNRAS*, 406, 782
- Swann E., 2020, *MNRAS*, in prep
- Taggart K., Perley D., 2019
- Tampo Y., et al., 2020
- Uno K., Maeda K., 2020, Technical report, Wind-Driven Transients as A Unified Model for Peculiar Events AT2018cow and iPTF14hls. ([arXiv:2003.05795v1](https://arxiv.org/abs/2003.05795v1))
- Vazdekis A., Sánchez-Blázquez P., Falcón-Barroso J., Cenarro A. J., Beasley M. A., Cardiel N., Gorgas J., Peletier R. F., 2010, *MNRAS*, 404, 1639
- Vergani S. D., et al., 2015, *A&A*, 581, A102
- Vergani S. D., et al., 2017
- Wiseman P., et al., 2020, *MNRAS*, submitted
- Woosley S. E., 1993, *ApJ*, 405, 273
- Woosley S. E., Bloom J. S., 2006, *Annu. Rev. Astron. Astrophys.*, 44, 507
- Woosley S. E., Heger A., 2006, *ApJ*, 637, 914
- Xu D., et al., 2018, *ATel*, 11740, 1
- York D. G., et al., 2000, *ApJ*, 120, 1579
- Yuan F., et al., 2015, *MNRAS*, 452, 3047
- Zahid H. J., Dima G. I., Kudritzki R.-P., Kewley L. J., Geller M. J., Hwang H. S., Silverman J. D., Kashino D., 2014, *ApJ*, 791, 130

Table A1. Emission line fluxes for DES RET host galaxies. Values are given in units of erg/cm/s/\AA , and have been corrected for Milky Way reddening using Schlegel et al. (1998), assuming a Cardelli et al. (1989) with $R_V = 3.1$, but not for intrinsic host galaxy reddening.

	[OII]3727	[OIII]4960	[OIII]5007	[NII]6549	[NII]6585	[SII]6717	[SII]6731	H δ	H γ	H β	H α
DES13X3gms	43.3 \pm 27.7	10.9 \pm 7.9	32.9 \pm 7.9	-	-	-	-	2.0 \pm 7.6	17.0 \pm 7.1	6.3 \pm 9.5	-
DES13C1tgd	1.9 \pm 0.7	0.0 \pm 0.1	0.0 \pm 0.1	0.5 \pm 0.1	1.6 \pm 0.1	1.1 \pm 0.0	0.8 \pm 0.0	0.9 \pm 0.2	1.3 \pm 0.1	0.2 \pm 0.1	4.5 \pm 0.2
DES13S2wxf	22.1 \pm 5.3	3.2 \pm 2.0	9.8 \pm 2.0	-	-	-	-	2.4 \pm 1.0	4.3 \pm 0.8	4.5 \pm 2.1	-
DES13X1hav	31.4 \pm 49.1	10.5 \pm 12.0	31.9 \pm 12.0	-	-	-	-	0.0 \pm 6.2	5.2 \pm 11.5	10.6 \pm 4.8	-
DES13X3nyg	15.1 \pm 1.6	3.2 \pm 0.4	9.8 \pm 0.4	-	-	-	-	0.5 \pm 0.4	0.0 \pm 0.6	3.3 \pm 0.4	-
DES13X3gmd	18.8 \pm 5.3	-	-	-	-	-	-	1.9 \pm 3.8	2.3 \pm 2.7	7.0 \pm 8.3	-
DES13X2wvv	61.5 \pm 14.4	7.4 \pm 3.6	22.6 \pm 3.6	-	-	-	-	2.7 \pm 4.9	1.1 \pm 3.3	10.3 \pm 2.8	-
DES14S2anq	486.0 \pm 0.4	74.9 \pm 1.1	227.1 \pm 1.1	10.3 \pm 5.1	31.1 \pm 5.1	43.1 \pm 4.0	31.1 \pm 4.5	31.5 \pm 1.4	58.9 \pm 1.4	114.0 \pm 1.4	240.0 \pm 0.9
DES14X1bnh	23.1 \pm 1.2	-	-	-	-	-	-	0.4 \pm 0.4	3.1 \pm 0.5	-	-
DES15S1fli	33.3 \pm 3.3	3.4 \pm 1.5	10.5 \pm 1.5	-	-	-	-	3.0 \pm 1.5	4.2 \pm 0.8	8.7 \pm 0.4	-
DES15S1flf	75.2 \pm 78.8	13.6 \pm 10.8	41.3 \pm 10.8	1.4 \pm 3.9	4.4 \pm 3.9	2.7 \pm 2.6	4.9 \pm 2.8	0.6 \pm 19.2	14.3 \pm 16.6	13.4 \pm 10.2	40.9 \pm 5.2
DES14X3pkl	13.5 \pm 9.5	2.6 \pm 0.8	7.9 \pm 0.8	0.7 \pm 0.4	2.2 \pm 0.4	3.5 \pm 0.5	1.9 \pm 0.3	1.7 \pm 2.7	2.6 \pm 2.8	0.0 \pm 2.1	10.4 \pm 0.7
DES13X3npb	14.6 \pm 4.1	1.4 \pm 0.2	4.2 \pm 0.2	-	-	-	-	2.3 \pm 0.2	4.0 \pm 0.2	5.7 \pm 0.2	-
DES15X2ead	9.7 \pm 10.0	0.8 \pm 0.8	2.3 \pm 0.8	0.8 \pm 0.4	2.5 \pm 0.4	3.5 \pm 0.3	2.2 \pm 0.6	2.9 \pm 2.5	1.3 \pm 1.7	2.3 \pm 0.8	11.5 \pm 0.3
DES14S2plb	14.1 \pm 0.7	1.0 \pm 0.1	3.0 \pm 0.1	1.2 \pm 0.0	3.6 \pm 0.0	2.3 \pm 0.0	1.8 \pm 0.0	2.0 \pm 0.1	2.3 \pm 0.1	4.8 \pm 0.1	12.2 \pm 0.0
DES14S2pli	13.7 \pm 0.9	0.6 \pm 0.1	1.7 \pm 0.1	-	-	-	-	0.0 \pm 0.4	1.6 \pm 0.3	3.5 \pm 0.1	-
DES14C3tnz	23.1 \pm 4.5	3.0 \pm 1.0	9.2 \pm 1.0	-	-	-	-	1.1 \pm 0.9	4.5 \pm 1.5	4.4 \pm 3.8	-
DES15X3mxf	29.5 \pm 3.4	1.7 \pm 0.5	5.2 \pm 0.5	-	-	-	-	1.1 \pm 2.8	4.0 \pm 1.2	5.0 \pm 0.5	-
DES15C3lpq	37.0 \pm 9.8	8.6 \pm 3.3	26.2 \pm 3.3	-	-	-	-	4.2 \pm 2.6	2.3 \pm 2.6	9.1 \pm 4.5	-
DES15C3nat	21.6 \pm 1.5	-	-	-	-	-	-	1.5 \pm 0.6	4.2 \pm 1.4	-	-
DES15C3mgq	17.0 \pm 20.8	6.3 \pm 2.4	19.1 \pm 2.4	0.4 \pm 1.3	1.3 \pm 1.3	1.2 \pm 0.7	0.0 \pm 3.6	1.8 \pm 5.1	1.7 \pm 4.0	6.2 \pm 2.9	10.6 \pm 0.8
DES15E2nqh	34.7 \pm 22.4	9.3 \pm 3.6	28.2 \pm 3.6	-	-	-	-	2.4 \pm 4.3	4.8 \pm 5.2	7.7 \pm 5.1	-
DES15C3opk	10.5 \pm 6.5	5.0 \pm 3.1	15.1 \pm 3.1	-	-	-	-	0.7 \pm 1.2	1.8 \pm 0.9	2.9 \pm 3.7	-
DES15C3opp	15.5 \pm 3.3	1.7 \pm 0.6	5.2 \pm 0.6	-	-	-	-	0.7 \pm 2.1	2.9 \pm 1.5	3.1 \pm 0.7	-
DES16E2pv	39.7 \pm 12.2	6.0 \pm 9.5	18.0 \pm 9.5	-	-	-	-	0.3 \pm 4.9	5.9 \pm 5.1	6.9 \pm 4.9	-
DES16S1bbp	37.2 \pm 13.0	7.5 \pm 1.7	22.9 \pm 1.7	0.7 \pm 0.4	2.1 \pm 0.4	2.8 \pm 1.3	2.0 \pm 0.4	2.9 \pm 2.7	6.0 \pm 1.9	12.2 \pm 2.3	24.2 \pm 0.8
DES16X3cxn	23.5 \pm 5.6	1.6 \pm 2.6	4.9 \pm 2.6	-	-	-	-	0.0 \pm 2.2	0.7 \pm 1.4	4.0 \pm 1.0	-
DES16C1cbd	9.3 \pm 1.8	0.6 \pm 0.3	1.8 \pm 0.3	-	-	-	-	0.8 \pm 0.1	1.0 \pm 0.1	1.9 \pm 0.1	-
DES16X3ega	28.2 \pm 2.1	0.9 \pm 1.0	2.8 \pm 1.0	1.0 \pm 0.8	3.0 \pm 0.8	2.8 \pm 0.4	1.5 \pm 0.9	2.0 \pm 0.8	4.4 \pm 0.7	5.8 \pm 0.5	14.5 \pm 0.4
DES16X3erw	31.6 \pm 4.0	2.9 \pm 1.6	8.8 \pm 1.6	-	-	-	-	3.4 \pm 1.7	2.1 \pm 1.5	7.2 \pm 0.7	-
DES16C3gin	17.1 \pm 2.8	1.5 \pm 0.4	4.4 \pm 0.4	-	-	-	-	1.6 \pm 1.1	0.0 \pm 1.2	4.3 \pm 0.6	10.1 \pm 0.5
DES16S1dxu	96.3 \pm 33.0	16.4 \pm 8.4	49.5 \pm 8.4	0.8 \pm 2.5	2.4 \pm 2.5	1.2 \pm 3.6	3.7 \pm 1.8	5.5 \pm 6.9	9.1 \pm 4.8	22.8 \pm 3.9	39.2 \pm 1.2
DES16X1eho	6.6 \pm 0.9	-	-	-	-	-	-	0.0 \pm 0.3	1.2 \pm 0.6	1.4 \pm 0.8	-
DES17C3gop	21.1 \pm 17.3	2.5 \pm 2.4	7.6 \pm 2.4	-	-	-	-	2.7 \pm 2.4	5.3 \pm 3.2	4.8 \pm 1.4	-
DES17S2fee	0.1 \pm 0.2	0.0 \pm 0.0	0.0 \pm 0.0	0.1 \pm 0.0	0.2 \pm 0.0	0.0 \pm 0.0	0.3 \pm 0.0	0.0 \pm 0.0	0.1 \pm 0.0	0.0 \pm 0.0	0.4 \pm 0.0
DES17X3dxu	22.1 \pm 2.8	-	-	-	-	-	-	3.8 \pm 6.1	4.7 \pm 1.3	-	-
DES17X3cds	9.4 \pm 6.5	2.0 \pm 1.1	6.1 \pm 1.1	-	-	-	-	0.0 \pm 0.9	0.6 \pm 0.7	3.1 \pm 0.7	-
DES17X3hxi	56.6 \pm 78.6	35.7 \pm 26.0	108.3 \pm 26.0	-	-	-	-	8.9 \pm 22.2	16.1 \pm 22.9	22.7 \pm 18.0	-
DES13E2lpk	11.3 \pm 0.7	0.5 \pm 0.1	1.5 \pm 0.1	-	-	-	-	0.7 \pm 0.2	1.3 \pm 0.1	3.3 \pm 0.1	-
DES15C2eal	28.1 \pm 17.9	2.1 \pm 2.3	6.5 \pm 2.3	0.5 \pm 1.6	1.5 \pm 1.6	3.0 \pm 0.7	4.3 \pm 0.8	0.0 \pm 4.4	4.0 \pm 3.7	4.1 \pm 3.2	17.6 \pm 2.0
DES16C2ggt	21.0 \pm 1.0	2.3 \pm 0.3	6.9 \pm 0.3	1.1 \pm 0.2	3.3 \pm 0.2	3.5 \pm 0.1	2.2 \pm 0.1	0.7 \pm 0.3	2.7 \pm 0.5	7.4 \pm 0.2	14.2 \pm 0.1
DES17C2hno	19.1 \pm 6.2	2.1 \pm 1.5	6.2 \pm 1.5	-	-	-	-	2.4 \pm 2.5	2.7 \pm 1.6	7.0 \pm 1.8	-

APPENDIX A: SPECTRAL LINE FLUXES

Table A1 presents the line fluxes for all DES RET hosts for which spectra were available.

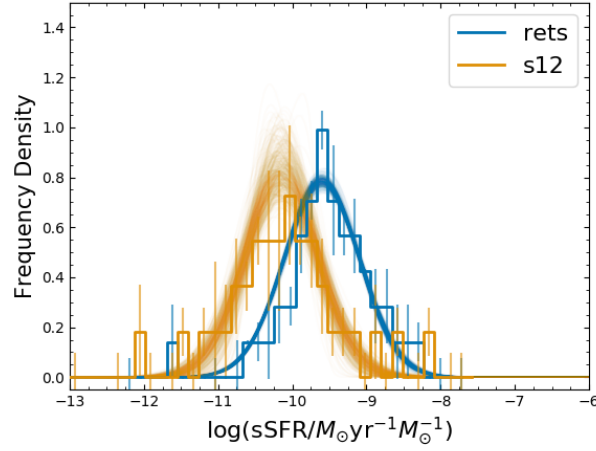


Figure B1. Results of the MCMC fits to the PDFs of sSFR for DES RETs and SESNe, accounting for uncertainties in each bin.

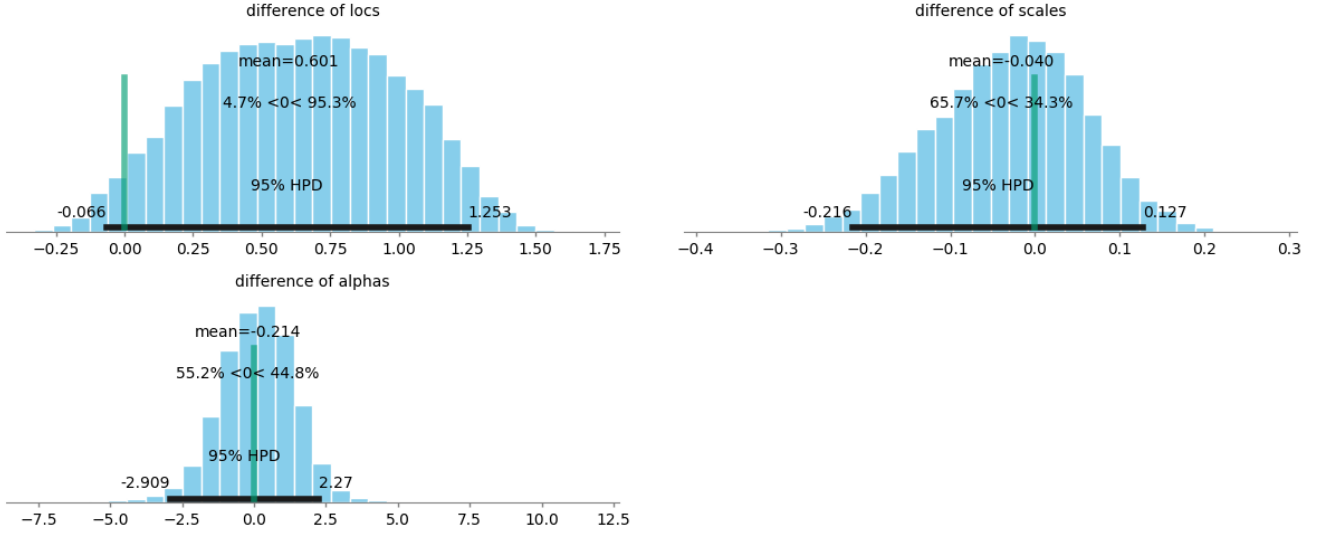


Figure B2. Histograms showing the differences between the fit parameters across the MCMC samples.

APPENDIX B: BAYESIAN FITS - SSFR

To compare two distributions we follow the method outlined in Wiseman et al. (2020). We fit the PDFs, along with the uncertainty on the value in each bin, simultaneously with the same priors using the No U-Turn Sampler (NUTS; Hoffman & Gelman 2014) Hamiltonian Monte Carlo algorithm via the pymc3⁴ package to explore the posterior distribution. We use a warm-up period of 5×10^3 iterations and a fit period of 10^4 iterations. Fig. C4 displays an example of the resulting fit where the DES RETs and Sanders et al. (2012) sSFR distributions are compared. Each resulting distribution is described by the ‘loc’ (location), ‘scale’ (spread), and ‘alpha’ (skewness). We then compare the differences in these parameters, as seen in Fig. B2, by reporting objectively the percentages of posterior samples that overlap, and subjectively what this means for the similarity of the distributions.

⁴ <https://docs.pymc.io/>

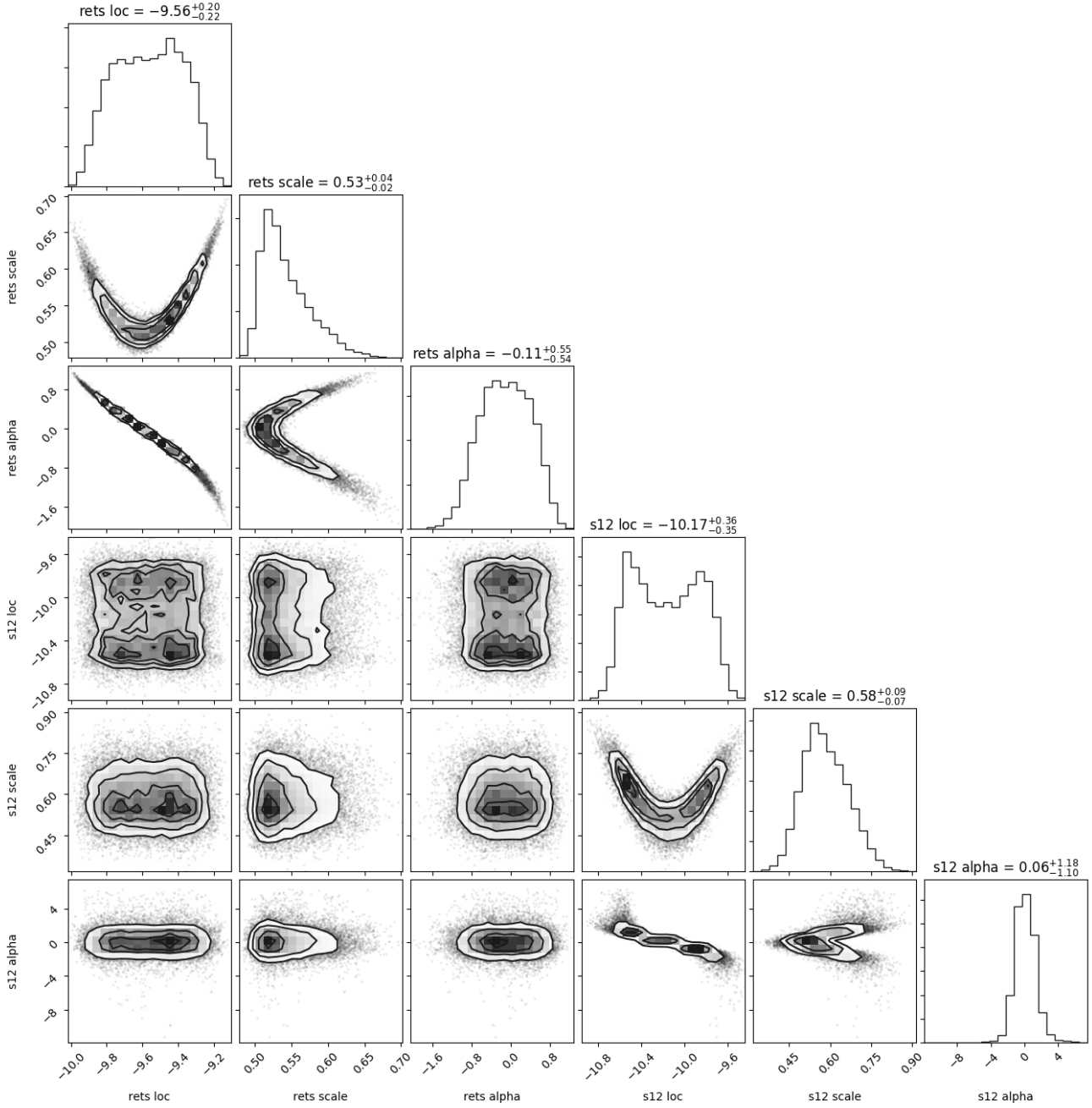


Figure B3. Corner plot showing the posterior samples from the MCMC fit to the DES RETs and Sanders et al. (2012) sSFRs. Notable features are: 1) the RET distribution is better constrained than the SESNe (S12); 2) the scale vs alpha and loc vs scale distributions are two-tailed due to alpha being centred close to 0; 3) there is a degeneracy between loc and alpha for the same reason. Figure produced using the *corner* package (Foreman-Mackey 2016).

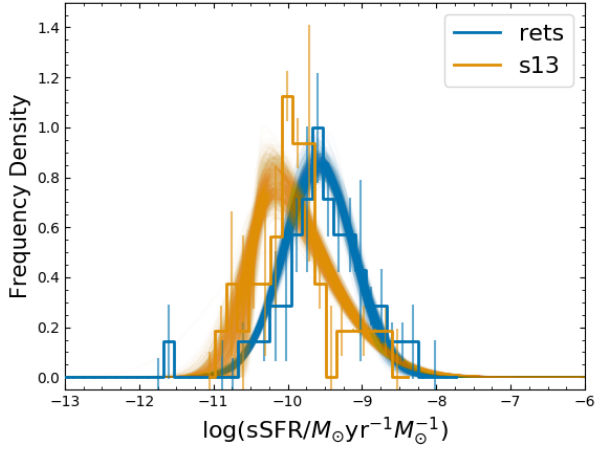


Figure B4. Results of the MCMC fits to the PDFs of sSFR for DES RETs and SNe II, accounting for uncertainties in each bin.

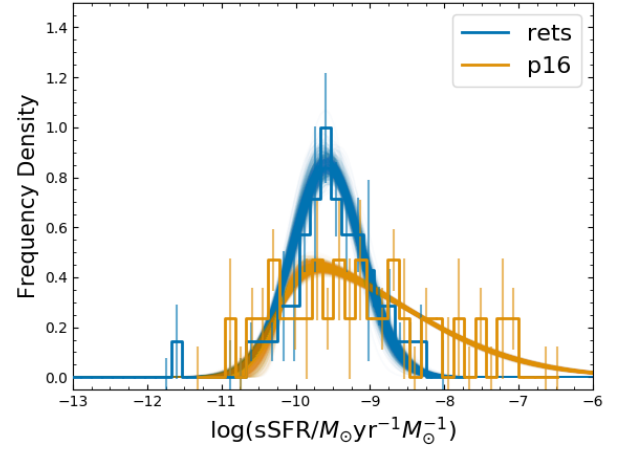


Figure B6. Results of the MCMC fits to the PDFs of sSFR for DES RETs and SLSNe, accounting for uncertainties in each bin.

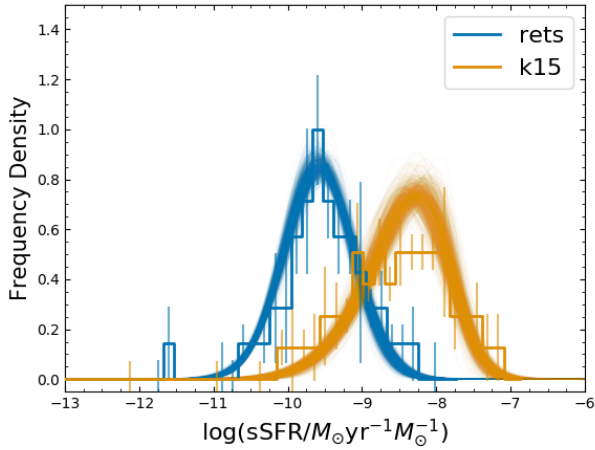


Figure B5. Results of the MCMC fits to the PDFs of sSFR for DES RETs and LGRBs, accounting for uncertainties in each bin.

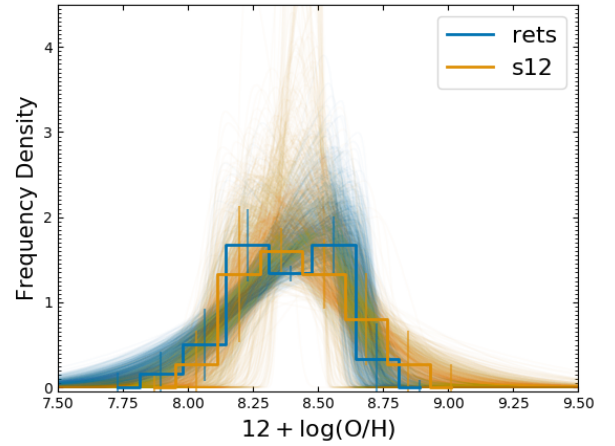


Figure C1. Results of the MCMC fits to the PDFs of metallicity for DES RETs and SESNe, accounting for uncertainties in each bin.

972 APPENDIX C: BAYESIAN FITS - METALLICITY

973 This paper has been typeset from a \LaTeX file prepared by the author.

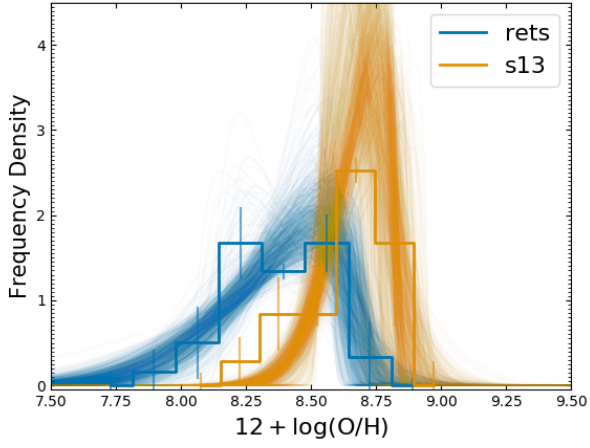


Figure C2. Results of the MCMC fits to the PDFs of metallicity for DES RETs and SNe II, accounting for uncertainties in each bin.

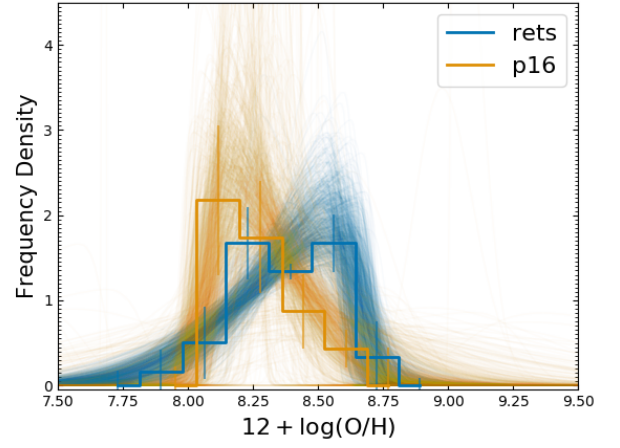


Figure C4. Results of the MCMC fits to the PDFs of metallicity for DES RETs and SLSNe, accounting for uncertainties in each bin.

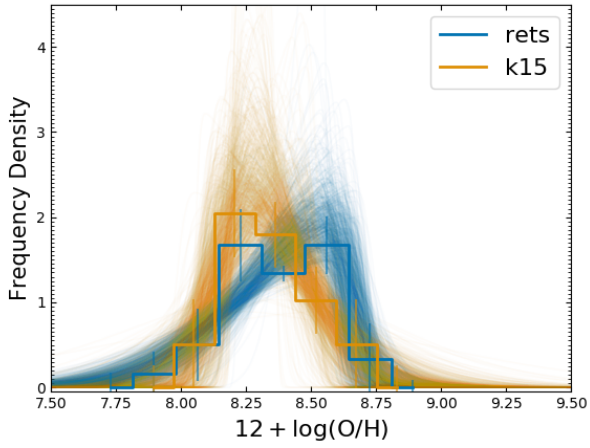


Figure C3. Results of the MCMC fits to the PDFs of metallicity for DES RETs and LGRBs, accounting for uncertainties in each bin.